Palaeogeography, Palaeoclimatology, Palaeoecology 563 (2021) 110169

Contents lists available at ScienceDirect

Palaeogeography, Palaeoclimatology, Palaeoecology

journal homepage: www.elsevier.com/locate/palaeo

# Geochemistry and molybdenum isotopes of the basal Datangpo Formation: Implications for ocean-redox conditions and organic matter accumulation during the Cryogenian interglaciation

Zhaozhao Tan [a,b], Wanglu Jia [a,*], Jie Li [c], Lu Yin [d,e], Susu Wang [a,b], Jinxiang Wu [a,b], Jianzhong Song [a], Ping'an Peng [a,b]

[a] State Key Laboratory of Organic Geochemistry, Guangzhou Institute of Geochemistry, Chinese Academy of Sciences, Guangzhou 510640, China
[b] University of Chinese Academy of Sciences, Beijing 100049, China
[c] State Key Laboratory of Isotope Geochemistry, Guangzhou Institute of Geochemistry, Chinese Academy of Sciences, Guangzhou 510640, China
[d] Key Laboratory of Regional Geology and Mineralization, Hebei GEO University, Shijiazhuang 050031, China
[e] College of Resources, Hebei GEO University, Shijiazhuang 050031, China

ARTICLE INFO

*Keywords:*
Black shale
Mn carbonate
Nanhua Basin
Sturtian glaciation
Oceanic anoxia
Nutrient elements

ABSTRACT

The basal Datangpo Formation in South China deposited in the Cryogenian interglacial period has gained increasing interest with the well development of organic-rich black shale and its hosted manganese (Mn) deposits (Mn carbonate), which contain important clues to the paleoclimate and ocean redox of this critical interval in Earth's history. The depositional environment of Mn deposits is still uncertain, as suggested by different suites of redox-indicating parameters. In addition, the Mn deposits are notable for their enrichment in organic matter (OM), despite the fact that the diagenetic origin for the Mn deposits would result in large consumption of OM. To gain insight into these issues, we present the geochemical and molybdenum (Mo) isotopic data of black shale and Mn carbonate samples from a new section. The Datangpo Mn carbonates are characterized by low Mo content (mostly <3.2 ppm) and slightly light Mo isotopic composition (mostly from +0.07‰ to +0.52‰), suggesting that Mo, once adsorbed in Mn-oxide particles, was released in suboxic or anoxic (non-sulfidic) pore water due to Mn-oxide reduction and then diffused back into the water column. Hence the extremely light Mo isotopic signatures might be rarely preserved in sediments. The Mn carbonate formation accompanied by OM re-mineralization within sediments may have caused lower total organic carbon (TOC) content relative to that in black shales. However, elevated nutrient input related with hydrothermal fluid activity probably enhanced primary productivity during the Mn deposition period. It is evidenced by: (1) the Mn-TOC-total inorganic carbon covariation displayed by the Datangpo section and (2) a positive correlation between TOC and Mn content when Mn content is higher than 10% in a large compiled dataset. A compilation of Mo concentration and Mo isotope data suggests that widespread anoxia prevailed during the Cryogenian interglaciation. Instead, Neoproterozoic ocean oxygenation was postponed to the Ediacaran.

## 1. Introduction

The Cryogenian Period (~720–635 Ma, namely the Neoproterozoic Snowball Earths, Hoffman et al., 2017)is a critical interval during the Neoproterozoic Oxidation Event (Och and Shields-Zhou, 2012; Planavsky et al., 2010). The breakup of the Rodinia Supercontinent and associated lengthening continental margins and intensified magmatic activity have been thought to enhance subaerial silicate weathering and draw down atmospheric $CO_2$ levels, triggering the global glaciations of the Cryogenian (Donnadieu et al., 2004). The Sturtian (~720–660 Ma) and Marinoan (~650–635 Ma) ice ages are the most representative global glaciations in the Cryogenian (Och and Shields-Zhou, 2012; Hoffman et al., 2017; Yu et al., 2020). The end of the Sturtian ice age may be related to climate warming caused by the continuous release of large amounts of $CO_2$ due to volcanic activity (Hoffman et al., 1998). A very high weathering rate in glaciated settings could have fertilized the oceans with abundant phosphate (Planavsky et al., 2010), causing the increased burial of light organic carbon associated with high rates of

* Corresponding author at: Guangzhou Institute of Geochemistry, Chinese Academy of Sciences, 511 Kehua Street, Tianhe District, Guangzhou 510640, China.
*E-mail address:* wljia@gig.ac.cn (W. Jia).

https://doi.org/10.1016/j.palaeo.2020.110169
Received 28 July 2020; Received in revised form 4 December 2020; Accepted 5 December 2020
Available online 15 December 2020

primary productivity after the long-lived glaciations (Planavsky et al., 2010; Mills et al., 2011). The massive burial of reduced carbon must have been balanced by a net release of oxygen into the atmosphere, leading to the temporary oxygenation of the Cryogenian interglacial atmosphere and ocean (Planavsky et al., 2010; Zhang et al., 2015; Lau et al., 2017). As expected, organic-rich black shales have been frequently observed worldwide during these periods (Fig. 1). Therefore, the analysis of redox-sensitive elements and iron (Fe) speciation (Canfield et al., 2008; Li et al., 2012; Kunzmann et al., 2015; Sperling et al., 2016; Scheller et al., 2018), as well as molybdenum (Mo) and Fe isotopes (Zhang et al., 2015; Cheng et al., 2018; Scheller et al., 2018), has been performed on these shales to explore ocean redox conditions in this period. Some critical evidence for increasing ocean oxygenation after the Sturtian glaciation has been presented by notably increased Mo concentrations and Fe isotope values in the black shale from the Datangpo Formation in the Nanhua Basin of South China (Chen et al., 2015; Zhang et al., 2015). Therefore, there has been increasing interest on the study of this shale unit during the past three years (Yu et al., 2017; Cheng et al., 2018; Ye et al., 2018; Bao et al., 2018; Ma et al., 2019; Wei et al., 2020).

The Datangpo Formation is a typical interglacial stratum between the Sturtian and the Marinoan glaciations. This stratum is unique among its global counterparts for the development of a manganese (Mn) carbonate member (well known as giant Datangpo-type manganese deposits in China) underlying relatively thick black shale member in the basal formation. The formation of Mn carbonate by a diagenetic reduction of Mn oxides has special meaning for the Precambrian atmospheric/ocean oxygen content, since a strong oxidizing potential is required to form Mn oxides (Planavsky et al., 2014, 2018). Molybdenum (Mo) isotopes in ancient Mn-enriched sediments and deposits have been shown to be a powerful proxy for the assessment of ocean redox conditions in the past (Planavsky et al., 2014, 2018; Cabral et al., 2019). In addition, this proxy was also used in the study of the depositional conditions of modern Mn-enriched sediments (Hardisty et al., 2016; Scholz et al., 2018).

The depositional conditions of the Datangpo Mn carbonates is still in controversy. Very low molar $C_{org}/P$ ratios of Mn carbonates have been used to suggest a temporary oxic condition associated with episodic deep-water ventilations (Yu et al., 2016). In contrast, Fe speciation data that are one of the mostly useful proxies for deep-water redox seem to suggest an anoxic, but non-euxinic condition (Ma et al., 2019; Wei et al., 2020). To date, no Mo isotope analysis were performed on Mn carbonates from the Datangpo Formation. What's more, reaction with organic matter in the sediments converts the Mn-oxides to $MnCO_3$, (Calvert and Pedersen, 1996; Huckriede and Meischner, 1996), which leads to a notable decrease of total organic carbon (TOC) content in Mn carbonates relative to black shales (Ma et al., 2019; Wei et al., 2020). By contrast, the formation and reduction of Mn oxides are mediated by enhanced microbial activities (Yu et al., 2016, 2019), which may increase the TOC content of the sediments. This is best shown by Mn carbonates samples being also organic-rich, similar to interbedded and hosted shale (Yu et al., 2016). Thus far, the OM enrichment characteristics of the Mn carbonates in the Datangpo Formation have not been discussed in detail.

To resolve these problems, a set of samples of Mn carbonates and black shales from the Datangpo section (27°57′53″N, 108°54′50″E) of the Datangpo Formation has been compared in terms of their carbon contents and isotopes, elemental concentrations, and Mo isotopes. After compiling geochemical data, we focus on (1) discussing the depositional environment of the Mn carbonates and black shales and their implications for the oceanic redox conditions between the Snowball Earths and (2) determining main factors controlling the OM enrichment in the Mn carbonates of the Datangpo Formation.

## 2. Geological setting

The South China Craton consists of two terranes, the Yangtze Block and Cathaysia Block, which were amalgamated during the early Neoproterozoic. During the breakup of the supercontinent Rodinia from the activities of a large mantle plume, the Nanhua Basin developed as a rift basin at ~820 Ma between the Yangtze and Cathaysia blocks (Fig. 2A; Wang and Li, 2003) and evolved into a passive marginal basin after the Cryogenian (Jiang et al., 2011). Neoproterozoic strata in this basin are composed of three major units: the lower pre-Cryogenian siliciclastic units, the middle Cryogenian glacial and interglacial deposits, and the upper Ediacaran mixed carbonate-siliciclastic units (Jiang et al., 2011). The two former units generally thicken from the shelf facies in the northwest toward the basin facies in the southeast, similar to the variation in water depths.

Cryogenian strata consist of two glacial units and one interglacial unit: the Chang'an-Fulu-Gucheng/Tiesi'ao glacial unit at the lower part (Sturtian ice age), the interglacial unit Datangpo/Xiangmeng in the middle, and the upper glacial unit Nantuo (Marinoan ice age). The lower glacial unit is further divided into three sub-units: the lower diamictites of the Chang'an Formation, the middle-banded iron formations, and sandstones of the Fulu Formation, and the upper diamictites of the Gucheng/Tiesi'ao Formation. The interglacial Datangpo Formation,

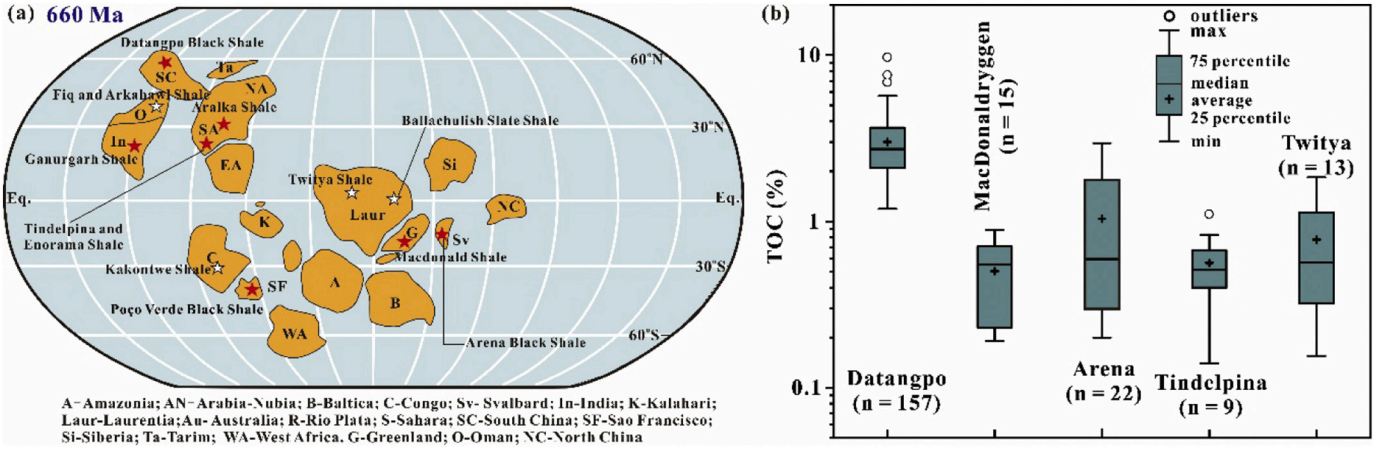


**Fig. 1.** (a) Paleogeographic reconstruction of the Cryogenian world (after Li et al., 2013 and Qi et al., 2018) and shale distribution between the Sturtian and Marinoan ice ages. (b) Whisker plots showing total organic carbon (TOC) contents of black shale at different intervals during the interglaciation: Poço Verd shale (Olcott et al., 2005), Arena shale (Kunzmann et al., 2015; Scheller et al., 2018), MacDonaldryggen shale (Kunzmann et al., 2015), Tindelpina shale (McKirdy et al., 2001; Kendall et al., 2006), Tapley Hill shale (McKirdy et al., 2001), Aralka shale (Schmid et al., 2018), Datangpo sediment, Fiq Formation shale (Rieu et al., 2007), Kaponda Shale, Nguba Group (Batumike et al., 2007), and Twitya shale (Sperling et al., 2016).

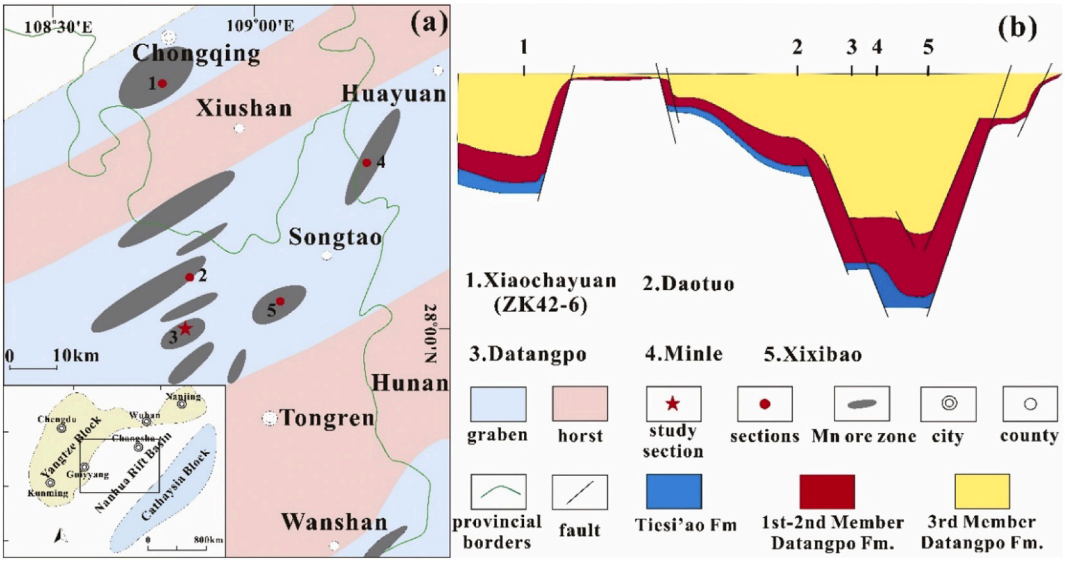


**Fig. 2.** (a) Paleogeography of the study area (after ; Zhou et al., 2004; Yu et al., 2016). The insert shows the location of the Nanhua Basin during the Cryogenian. (b) Cross-section for the post-Sturtian interglacial strata in the Nanhua Rift Basin (simplified after Yu et al., 2019).

conformably overlying the Tiesi'ao diamictites and underlying the Nantuo diamictites, is well constrained by a high-precision age of 660.98 ± 0.74 Ma near the base and by the age 657.17 ± 0.78 Ma near the top (Rooney et al., 2020 and references therein). During the deposition of Datangpo Formation, the Nanhua Basin was likely a restricted basin with limited seawater exchange with the open sea, depending on the variation in the sea level (Wang and Li, 2003; Li et al., 2012). This feature might be common for rift basins worldwide during the interglacial period (Li et al., 2012).

The thickness of the Datangpo Formation in outcrops and drill cores varies greatly from 10 to 700 m (Li et al., 2012; Yu et al., 2016), which was controlled by the paleobathymetry of the Nanhua Basin consisting of a series of northeast-southwest trending horsts and grabens, together with uncertain glacial erosion (Fig. 2A; Yu et al., 2016, 2017). Nevertheless, the lithological characteristics are similar for the sections deposited at different water depths (Fig. 2B; Li et al., 2012; Yu et al., 2016). The Datangpo Formation can be divided into three major members from bottom to top (Yu et al., 2016): the first member, black Mn carbonates interbedded with black shale and Mn shale (a few meters); the second member, black shale in the middle (a few tens of meters); the third member, the grey shale and siltstone in the upper part (a few hundreds of meters).

## 3. Samples and methods

### 3.1. Organic and inorganic carbon

A total of 33 samples were collected from a 10.5 m section comprised of the majority of Members 1 and 2 of the Datangpo Formation (Fig. 3), located within the Datangpo mining area in Songtao County (northeast

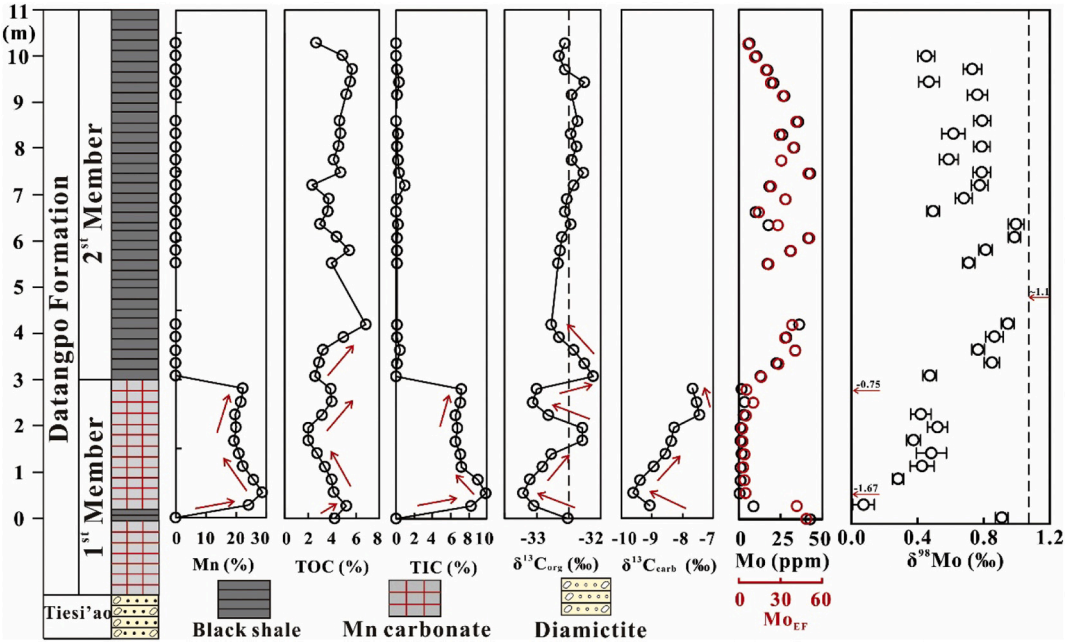


**Fig. 3.** Stratigraphic distribution of Mn, total organic carbon (TOC), and total inorganic carbon (TIC) content, isotopic composition of carbon ($\delta^{13}C_{org}$, and $\delta^{13}C_{carb}$), as well as the Mo content and $\delta^{98}$Mo composition. The $\delta^{98}$Mo value of ~1.1‰ occurred in euxinic shale (referenced from Cheng et al., 2018).

Guizhou Province, China). Relatively small sample blocks without visible veins and pyrite accumulates were selected, and their weathered surfaces were polished off with 80-mesh quartz sandpaper and then washed with Milli-Q water. The dried samples were first crushed to 0.25 cm pieces by a corundum crusher and further milled to less than 200 mesh in an agate mortar. All of the following analyses were performed at the Guangzhou Institute of Geochemistry, Chinese Academy of Sciences.

Raw and de-carbonated samples (with 5% HCl at 80 °C overnight) were analyzed by an Eltra CS800 carbon/sulfur analyzer for the total carbon (TC) and TOC content, respectively. About 80 mg of sample powder were weighed into crucibles and combusted in pure (99.95%) $O_2$ at 1350 °C. The precision was better than 0.2‰ based on the analysis of a standard AEB2178. Total inorganic carbon (TIC) content was determined to be the difference between TC and TOC contents.

$\delta^{13}C_{carb}$ analyses were carried out using a Delta$^{Plus}$ XL (Thermo Fisher Scientific) isotope ratio mass spectrometer (IRMS) interfaced to a carbonate preparation device via a GasBench II interface. The standard GBW-04405, with a $\delta^{13}C$ value of +0.57 ± 0.03‰ (VPDB), was used for calibration during the analysis. Due to negligible TIC content in black shales, only Mn carbonates were analyzed. Analytical precision is better than 0.1‰ for $\delta^{13}C_{carb}$ (VPDB). Organic carbon isotope ($\delta^{13}C_{org}$) was measured on the decarbonated (5% HCl treatment overnight) samples using a Thermo Finigan Delta$^{Plus}$ XL IRMS instrument coupled to a CE Flash-1112 element analyzer via a Confo III interface. CASEIN with a $\delta^{13}C$ value of −26.98‰ (VPDB) was used for calibration. The precision of was better than 0.2‰ (VPDB). All carbon isotopes in samples were routinely measured in duplicate, and the average value was used for discussion.

### 3.2. Major and trace elements

About 1 g of sample powder was mixed with 11 g of $Li_2B_4O_7$-$Li_2BO_2$ latent solvent in a platinum crucible and heated to 1100 °C in a furnace, then cooled to produce a glass disk for major element analysis. Major element concentrations were determined using a Thermo Scientific Fisher ARL 9900 X-ray fluorescence spectrometer. Analytical precision was usually better than 3%. Three rock standards, including RGM-2, BCR-2, and BHVO-2, were used for calibration.

Before trace element analysis, the sample powders were ashed at 650 °C to remove organic matter and digested in $HNO_3 + HF + HClO_4$ in Teflon pressure vessels to dissolve refractory minerals. Trace elements were analyzed by ICP–MS (Thermo iCAP Qc). An internal standard (Rhodium) was used to monitor and correct the signal drift of the instrument during the measurements. Seven standard rock samples were calibrated, including three international standards of W-2A, BHVO-2, and AGV-1, and four Chinese standards of GSD-9, GSR-1, GSR-2, and GSR-3. The precision is better than ±5%.

### 3.3. Mo contents and stable isotopes

The double-spike method used for the determination of Mo contents and isotopic compositions has been reported by Li et al. (2014). Mo separation and purification were achieved using an extraction chromatographic resin of N-benzoyl-*N*-phenyl hydroxylamine manufactured in-house following the protocols of Li et al. (2014). After the sample matrix and interference elements were removed, Mo isotope measurement was performed on a Thermo-Fisher Scientific Neptune-Plus multi-collector inductively coupled plasma mass spectrometer (MC–ICP–MS) utilizing double spike analysis to correct for instrumental mass bias (Siebert et al., 2001). Isotope measurements are made relative to a NIST SRM 3134 standard solution and then recalculated relative to the Johnson Matthey Specpure Mo plasma standard set to +0.25‰ for international comparison (Nägler et al., 2014). The external reproducibility of the NIST SRM 3134 standard solution is at 0.06‰ (2SD, $n = 20$) for the $\delta^{98/95}$Mo values. The United States Geological Survey black shale reference materials SGR-1b and IAPSO seawater standard were simultaneously processed with each batch of samples to monitor accuracy and gave the $\delta^{98/95}$Mo value of +0.65 ± 0.05‰ and + 2.30 ± 0.09‰ (2 SD, $n = 4$), respectively. Repeat measurement of IAPSO seawater standard over the course of half years yielded a reproducibility of 2.31 ± 0.09‰ (2SD; $n = 24$). The Mo procedural blank was <0.1 ng, much less than the Mo contents in the samples.

## 4. Results

According to Mn contents, collected samples could be classified into two members (Fig. 3): Mn carbonates with Mn content >20% in the lower part and black shale with trace Mn content (<0.1%) in the middle-upper part. The shale sample underlying Mn carbonates did not show substantial distinctions from other black shales.

### 4.1. Carbon content and isotopes

Both the Mn carbonate and black shale samples containe abundant OM, as indicated by relatively high TOC contents of 2.00–6.88 wt% (average 4.02 wt%, Table S1 and Fig. 3). The TOC contents in Mn carbonates (average 3.45 wt%, $n = 10$) are slightly lower than those in black shales (average 4.26 wt%, $n = 23$). TIC contents in the Mn carbonates vary from 6.50 to 9.83 wt% (Table S1, average 7.54 wt%) and show clear co-variations with Mn contents, consistent with the dominance of rhodochrosite in Mn-bearing minerals (Yu et al., 2016, 2019). In addition, TOC contents closely correlate with the Mn and TIC contents for the Mn carbonates, i.e. first decrease from the bottom to the middle part of Mn carbonate member, then increase to the top (shown by red arrows, Fig. 3). By contrast, TIC contents of black shales are very low and vary little with TOC contents.

$\delta^{13}C_{org}$ values of all the samples show an overall small variation (from −33.2‰ to −32.1‰, Table S1, Fig. 3), and they are slightly heavier for black shales than Mn carbonates. Interestingly, $\delta^{13}C_{org}$ values of Mn carbonates and shales within the lower 4.5 m part of the section show the reverse trend for TOC contents, i.e. three cycles of decrease-increase upwards (Fig. 3). Coming into the upper 4.5 m part of the section, the $\delta^{13}C_{org}$ values of shale samples vary little. The $\delta^{13}C_{carb}$ values of Mn carbonates vary from −9.6‰ to −7.4‰ (Table S1), which is similar to previously reported results (Yu et al., 2017). From the bottom to the top, $\delta^{13}C_{carb}$ values first decrease followed by an increasing trend, which is generally consistent with variations of $\delta^{13}C_{org}$ values. However, $\delta^{13}C_{carb}$ values of the uppermost three Mn carbonates did not show a negative shift again, which is different from $\delta^{13}C_{org}$ values of these samples.

### 4.2. Mo content and isotope composition

The contents of Mo in black shales vary from 6 to 43 ppm (average 26 ppm, Fig. 3). By contrast, they vary from 0.6 to 8.8 ppm (average 2.1 ppm) in Mn carbonates. The $Mo_{EF}$ of black shales vary from 6 to 51 and from 2 to 10 in Mn carbonates (with one sample having high value of 42) (Table S2, $EF_{sample} = (X/Al)_{sample}/(X/Al)_{PAAS}$ (Tribovillard et al., 2006), post-Archean Australia average shale (PAAS) composition inferenced from Taylor and McLennan (1985)). The $\delta^{98}$Mo values of studied samples range from −1.67 to +1.0‰ (Table S2, Fig. 3). The $\delta^{98}$Mo values of the Mn carbonates are variable and overall low, ranging from −1.67 to +0.52‰, below that of average oceanic input (~ +0.7‰) (Archer and Vance, 2008). By contrast, the black shales display relatively high $\delta^{98}$Mo values (from +0.45‰ to +1.0‰, Fig. 3).

### 4.3. Nutrient elements

The contents of nutrient related elements (Fe, P, Cu, Zn, and Ni) in the Mn carbonates and black shales are listed in Table S2 and S3. Fe and Cu contents in black shales vary from 0.51 to 4.04 wt% (average 2.53 wt %) and from 4 to 99 ppm (average 44 ppm), which are close to that in

Mn carbonates (Fe: 1.55–3.49 wt%, average 2.43 wt%; Cu:11–67 ppm, average 43 ppm). However, P, Zn, and Ni contents in black shales range from 0.02 to 0.12 wt% (average 0.05 wt%), from 17 to 65 ppm (average 34 ppm), and from 3 to 89 ppm (average 29 ppm), respectively, which are lower than those in Mn carbonate samples (P: 0.15–0.41 wt%, average 0.28 wt%; Zn: 52–213 ppm, average 104 ppm; Ni: 27–49 ppm, average 37 ppm). The values of $Fe_{EF}$, $P_{EF}$, $Cu_{EF}$, $Zn_{EF}$, and $Ni_{EF}$ in black shales are obviously lower than that in Mn carbonate (Fig. 4).

### 4.4. Rare earth elements (REEs)

The total REE (∑REE) content in Mn carbonates range from 200 to 271 ppm (average 236 ppm), but in black shales, it has a larger range from 135 to 602 ppm (average 248 ppm). When normalized to PAAS (Fig. 5), almost all of the samples show REE enrichment relative to PAAS. Mn carbonates show light REE and heavy REE depleted but mid-REE enriched patterns, while black shales show overall flat REE patterns with only a few samples having light REE-enrichment. Moreover, positive Ce and Eu anomalies are common in the Mn carbonates, ranging from 1.13 to 1.44 and from 1.05 to 1.41, respectively. By contrast, a negative Eu anomaly (Eu/Eu*) was commonly observed in black shales samples, ranging from 0.66 to 0.95 (average 0.83, Table S4).

## 5. Discussion

### 5.1. Hydrothermal activity and the nutrient-related elements in Mn-carbonates

Hydrothermal fluid is another important source for Mn ore deposits throughout geological history in addition to silicate weathering (Roy, 2006; Polgári et al., 2012; Maynard, 2014). This is very likely for some Neoproterozoic manganese deposits always formed in the interglacial stages of rift basins (Roy, 2006). The contribution from hydrothermal sourced Mn to the Datangpo Mn carbonates has been demonstrated by a combination of element contents with Sr and Nd isotopes (Wu et al., 2016; Yu et al., 2016). Two lines of elemental evidence obtained in this study are consistent with previous conclusions: 1) a positive correlation between Eu/Eu* and Mn content, as positive Eu anomalies are characteristic of hydrothermal fluids (Peter and Goodfellow, 1996, Fig. 6a); (2) the plots Fe/Ti versus Al/(Al + Fe + Mn) clearly suggest that hydrothermal fluid has the greatest contribution to Mn carbonates, medium to Mn-rich shales, and the least to black shales. Mn carbonate samples fall within the hydrothermal field, indicating the Mn interval exhibits the greatest hydrothermal influence (Marchig et al., 1982; Boström, 1983, Fig. 6b).

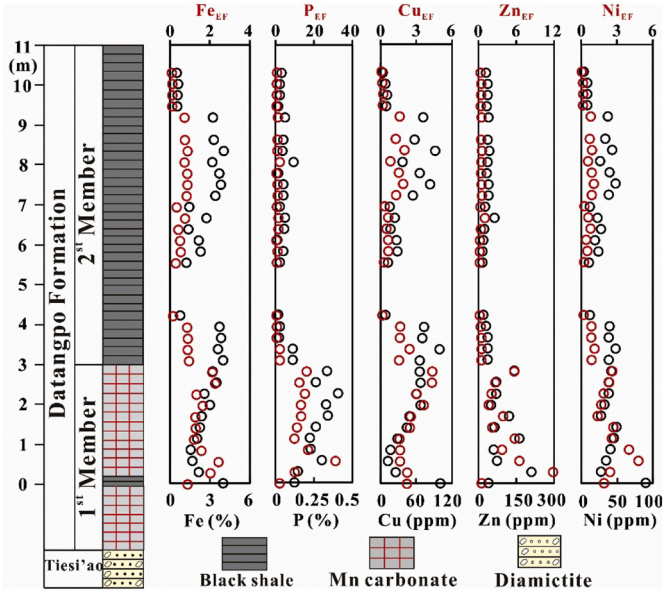


**Fig. 4.** Stratigraphic profiles of element contents for nutrient related elements.

Strong deep hydrothermal activity brought mantle or deep crustal materials into seawater, providing essential nutrients (Fe, Mn, Cu, Zn, and Ni) to promote the massive breeding of microorganisms and greatly increase OM productivity (Tribovillard et al., 2006; Dick et al., 2013). In the modern submarine-hydrothermal plumes, sediments associated with fluid events contained high levels of Fe, Mn, Co, Cu, Ni, Pb, and Zn relative to typical marine sediments (Shanks and Bischoff, 1977; Laurila et al., 2015; Hung et al., 2018). Similarly, such high concentrations of metalliferous sediments, which are likely sourced from hydrothermal activity, might provide a Precambrian record of ocean chemistry (Planavsky et al., 2011, 2018). Consistent with these modern and ancient analogues, the contents of several major and trace elements, Fe, Cu, Zn, Ni, and Co, generally increase with Mn content (Fig. 7). Therefore, hydrothermal activities likely made a large contribution to the nutrient-related elements in Mn-carbonates. Nevertheless, other factors, such as the local redox conditions and weathering effects, could also be possible candidates and should be evaluated carefully.

Compared with black shale, the high EF factors ($Fe_{EF}$, $Cu_{EF}$, $Zn_{EF}$, $Co_{EF}$, and $Ni_{EF}$) in the Mn-carbonate samples (Fig. 7) are probably not associated with the differences in the redox conditions. The high Fe enrichment of sediments, as proxied by the Fe/Al ratio can be used as an indicator for anoxic bottom water (Raiswell et al., 2018), while Mo, Zn, Co, Cu, Ni, and Pb are associated with sulfides, typically pyrites (Algeo and Liu, 2020; Scott et al., 2008). Therefore, relatively high contents of these elements, i.e. Fe, Cu, Zn, Co, and Ni, can be generally used to indicate anoxic conditions. By contrast, relative P content would be high in more oxic conditions, and molar $C_{org}/P$ ratio thus shows good covariation with the EF factors of trace metals (Algeo and Liu, 2020). There is still no consensus about the redox conditions during the Mn carbonate deposition of the Datangpo Formation; however, the upper black shale has been well demonstrated to have been deposited under euxinic conditions (Li et al., 2012; Cheng et al., 2018; Ma et al., 2019). As a result, EF factors ($Fe_{EF}$, $Cu_{EF}$, $Zn_{EF}$, $Co_{EF}$, and $Ni_{EF}$) in the black shales should exceed or at least equal the Mn-carbonate samples, which seems to be the opposite of our results (Fig. 7). Although effects of oxic or suboxic conditions on the P enrichment could be possible, higher EF values of P in Mn carbonates (as high as 35, Fig. 7f) than those of trace metals could be partly related to a hydrothermal input.

Weathering effects on the nutrient input could be assessed by the chemical index of alteration (CIA), which has been applied to evaluate the degree of chemical weathering and climate changes during the Cryogenian interglaciation (Wang et al., 2020). Major element CN–K–Al ternary plots (Fig. 8a), showing an ideal straight line parallel to the A-CN sideline in response to variable weathering intensity (Taylor and McLennan, 1995), reveal that the basal Datangpo sediments are less affected by K-metasomatism. According to Nesbitt and Young (1982) and McLennan (1993), the calculated CIA values ($CIA = 100 \times Al_2O_3/(Al_2O_3 + CaO^* + Na_2O + K_2O)$ in molar quantities) of the Datangpo black shales and Mn carbonates mostly vary from 60 to 80. Among these sample series, CIA values are the highest for black shales, moderate for Mn shales, and the least for Mn carbonates (Fig. 8b), which may suggest enhanced weathering during the deposition of black shale (Wang et al., 2020). A significant negative $\delta^7Li$ excursion for the black shales from the Mn carbonate interval also suggests enhanced silicate weathering intensity and nutrient flux during this period (Wei et al., 2020). By contrast, the greater enrichment of nutrient elements of Mn carbonates than black shales are not related to a weathering effect, but submarine hydrothermal fluids.

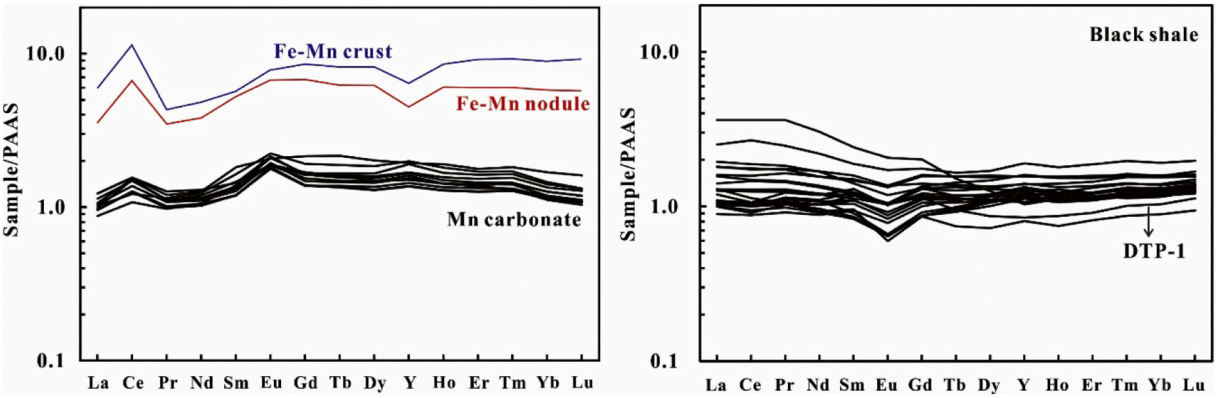


**Fig. 5.** PAAS-normalized REE patterns of samples from Mn carbonate and black shale. For comparison, modern marine ferromanganese deposits are also plotted (Bau et al., 2014).

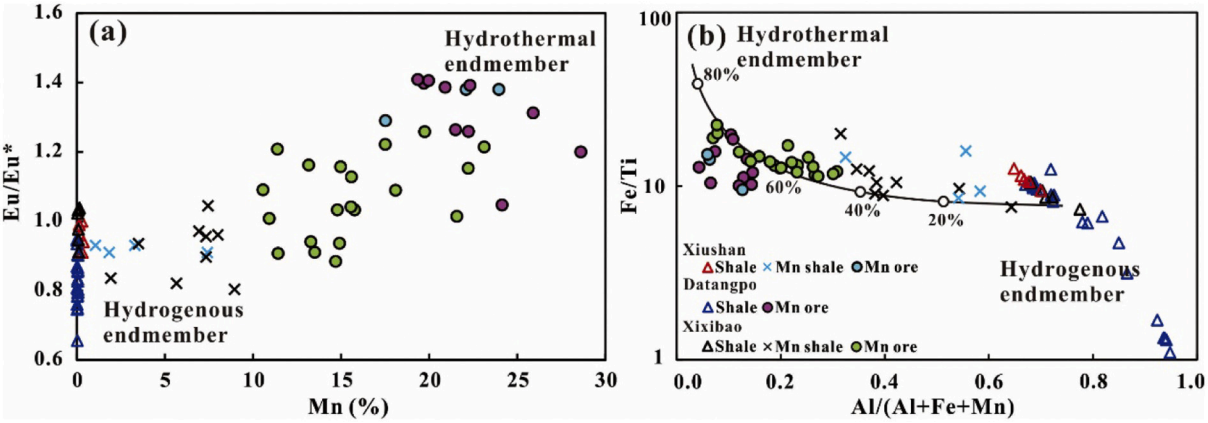


**Fig. 6.** Discriminant plots of sediments with hydrothermal and hydrogenous origins. (a) Eu/Eu* versus Mn (Peter and Goodfellow, 1996). (b) Al/(Al + Fe + Mn) versus Fe/Ti shows percent composition from hydrothermal (Marchig et al., 1982; Boström, 1983). Xiaochayuan (ZK43-6) data at Xiushan are from Ma et al. (2019); Datangpo Section data are from this study; and Xixibao data are from Yu et al. (2016).

### 5.2. Redox conditions suggested by Mo content and isotopes

#### 5.2.1. Redox during black shale deposition

Mo is present as a stable, unreactive molybdate anion ($MoO_4^{2-}$) in a water solution in the oxic conditions (Algeo and Lyons, 2006), and thus little enriched in the sediments deposited under this condition. In the presence of free $H_2S$ in the bottom water or sediment pore fluids, $MoO_4^{2-}$ is efficiently converted to particle-active thiomolybdates [$MoO_xS_{4-x}^{2-}$(x = 0 to 3)] (Helz et al., 1996). A post-thiomolybdate step from Mo(*VI*) $OS_3^{2-}$ to Mo(*IV*)$O(S_4)S^{2-}$ or Mo(*IV*)$S(S_4)S^{2-}$ may occur in the euxinic sediments or the water column (Dahl et al., 2013). These thiomolybdates and Mo(IV)-polysulfides are prone to being absorbed by OM and metal sulfides (such as pyrites, Helz et al., 1996; Tribovillard et al., 2004) or undergoing equilibrium precipitation as Fe(II)-Mo(VI) sulfides (Helz et al., 2011). These processes thus remove Mo from seawater and result in Mo enrichment in euxinic black shales.

As best shown by Fe speciation (Li et al., 2012; Ma et al., 2019; Wei et al., 2020), the euxinic conditions dominates the main deposition period of the Datangpo black shales (Fig. 9), and the persistence and intensity of euxina are more pronounced in deep-water facies than shallow water ones (Li et al., 2012). Black shales deposited under the euxinic conditions usually show notable Mo enrichment, which is also influenced by seawater Mo availability, including the Mo concentration in the global ocean and the restriction of local basins (Algeo and Lyons, 2006). The Mo content of the black shales obtained in this study (6–43 ppm) falls within the range defined by a large previous dataset, which is consistent with mainly euxinic conditions, but an overall small Mo reservoir during the Cryogenian interglacial period (Li et al., 2012; Ye et al., 2018; Ma et al., 2019; Wei et al., 2020).

In euxinic conditions, Mo isotopic fractionation is closely related to aqueous $H_2S$ concentrations ($[H2S]_{aq}$), and a positive correlation is observed between $\delta^{98}$Mo and $[H_2S]_{aq}$ (Neubert et al., 2008; Poulson Brucker et al., 2009). The $\delta^{98}$Mo values obtained for black shales in this study (from 0.45‰ to 1.0‰) fall within the previously reported ranges (Cheng et al., 2018; Fig. 10). Although the Fe speciation proxy indicates a prevailing euxinic bottom water for Minle black shales, and $Fe_{py}/Fe_{HR}$ values fluctuating around 0.7 may be associated with transient redox variations, especially changes in $[H_2S]_{aq}$. Therefore, Cheng et al. (2018) attributed higher $\delta^{98}$Mo values (+1.06‰ ± 0.06‰) to be associated with stable and high seawater $H_2S$ content ($[H_2S]_{aq}$ above 11 μM), and lower $\delta^{98}$Mo values (−0.13‰ to 0.68‰) with weakly euxinic conditions. Similar to Cheng et al.'s (2018) data, a moderate linear correlation of $\delta^{98}$Mo values with $Mo_{EF}$ is observed in the Datangpo section, suggesting that the basal Datangpo black shales were deposited under euxinic conditions with unstable seawater $[H_2S]_{aq}$ (Fig. 10).

#### 5.2.2. Redox during Mn carbonate deposition

Compared to the black shales, the depositional environment of Mn carbonates in the basal Datangpo Formation is not well constrained yet. This issue is mainly related to the inconsistences between several suits of redox-sensitive parameters: very low molar $C_{org}/P$ ratios and Mo content of Mn carbonates suggest oxic and suboxic conditions, respectively (Yu et al., 2016; Ma et al., 2019), but Fe speciation data clearly suggest a ferruginous (non-euxinic) condition (Ma et al., 2019; Wei et al., 2020).

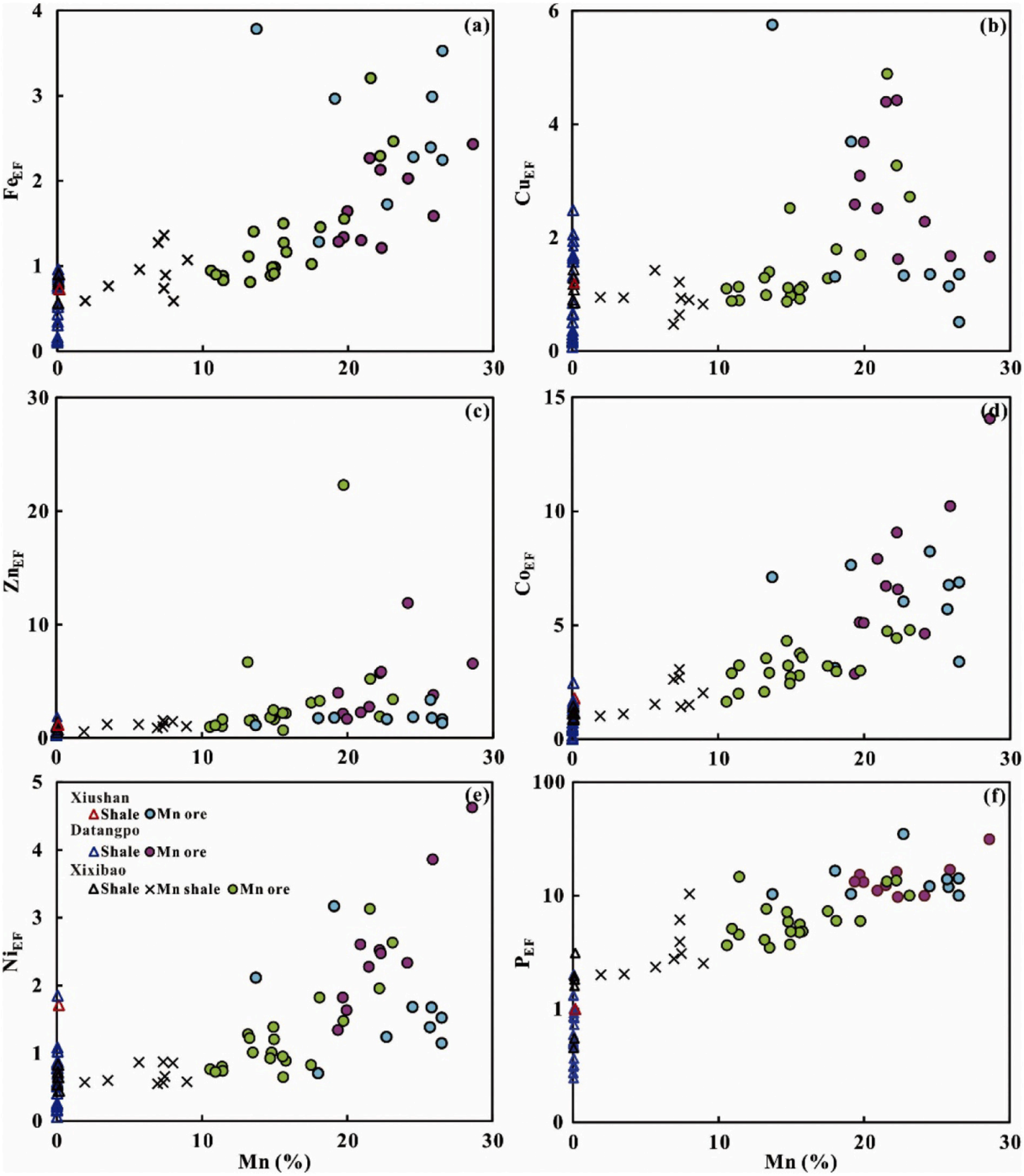


**Fig. 7.** Relationship between Mn content with $Fe_{EF}$, $Cu_{EF}$, $Zn_{EF}$, $Co_{EF}$, $Ni_{EF}$, and $P_{EF}$. Xiushan data are from Wu et al. (2016); Datangpo Section data are from this study; and Xixibao data are from Yu et al. (2016).

As mentioned above (Fig. 7), both P and Fe contents in Mn carbonates have been influenced by hydrothermal fluids to higher values than those in black shales. Therefore, $C_{org}$/P ratios and Fe speciation data of Mn carbonates might have been altered, due to the hydrothermal effect. Rarely affected by hydrothermal fluids, the Mo content in Mn carbonates could be mainly related to the local redox. Therefore, the Mo contents and Mo isotopes were mainly explored for their redox implications for Mn carbonates from the Datangpo Formation, as shown to be effective in two recent studies, one on Paleoproterozoic Morro da Mina Mn-ore deposits and another on modern Mn-enriched sapropel in the Baltic sea (Hardisty et al., 2016; Cabral et al., 2019).

The Datangpo Mn carbonates share two major similarities with the Morro da Mina Mn-ore (queluzite ore) and the Baltic sapropel (Fig. 11a, b): (1) High OM enrichment; (2) The main Mn-containing mineral is Mn carbonate. Having evolved into the greenschist metamorphic stage, the queluzite samples are mainly composed of Mn carbonates with some Mn silicates (Cabral et al., 2019). The modern Baltic sapropels, though the minerals were not analyzed, show positive linear correlation between Mn and TIC contents, and thus have Mn carbonate as the major Mn containing mineral (Hardisty et al., 2016). However, two major differences exist. First, both the Morro da Mina Mn-ore and the Baltic sapropel samples are highly Mo enriched (mostly higher than 10 ppm and up to a few hundreds of ppm, Fig. 11c); by contrast, the Datangpo Mn carbonates are evidently Mo depleted. Second, the three units show different

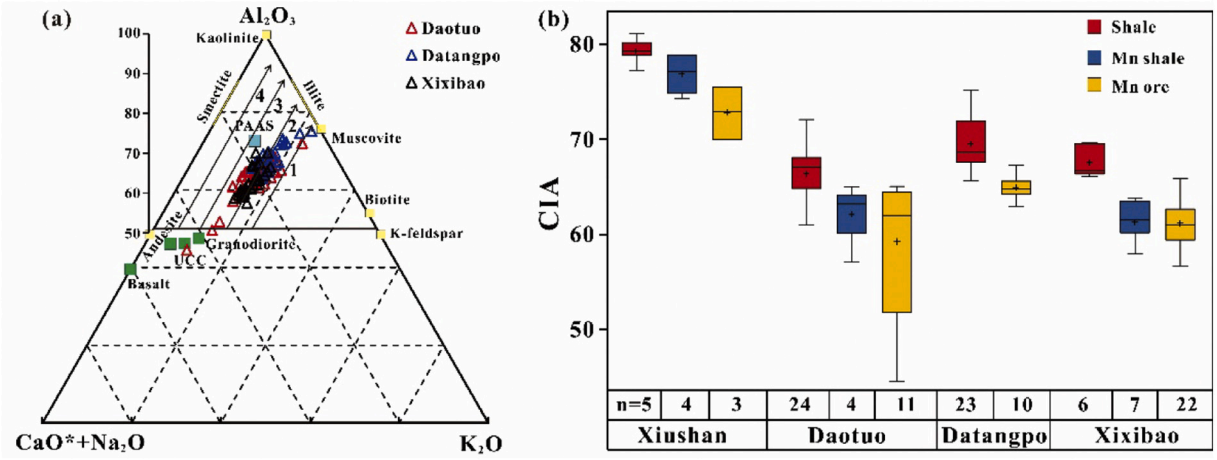


**Fig. 8.** (a) Chemical weathering ternary diagram after Taylor and McLennan (1995) showing what could be interpreted as a chemical weathering trend. Numbers 1–4 represent compositional trends of initial weathering profiles for different rocks: 1 granite, 2 monzogranite, 3 granodiorite, 4 tonalite. (b) Whisker plots showing CIA values distribution of shale, Mn shale, and Mn ore samples in different sections from Nanhua Basin. Xiushan data are from Ma et al. (2019); Daotuo data are from Zhang et al. (2015); Datangpo Section data are from this study; Xixibao data are from Yu et al. (2016).

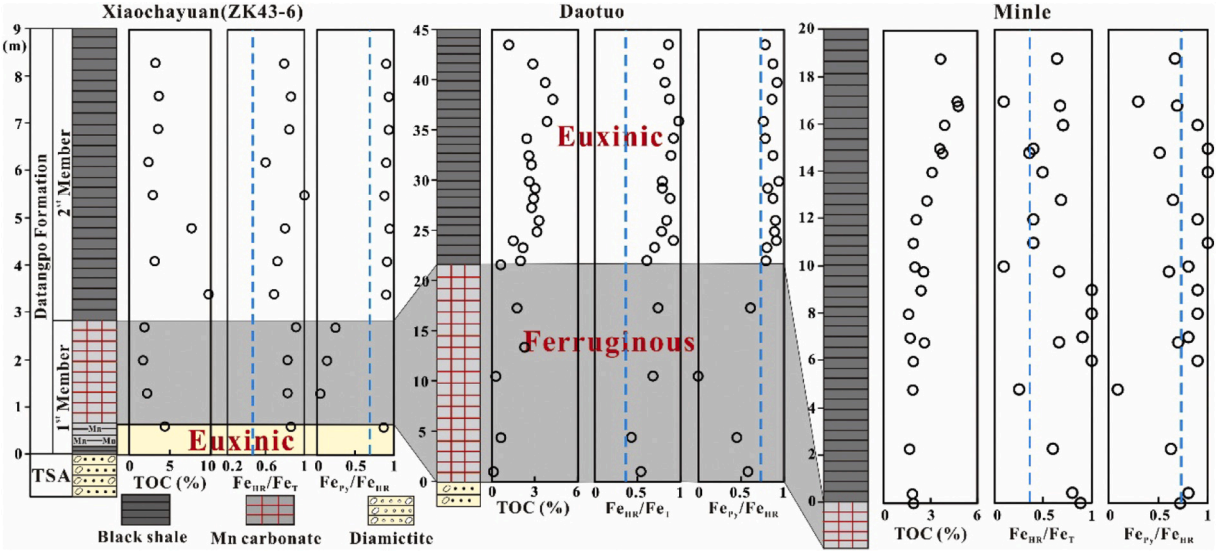


**Fig. 9.** Compiled data of iron speciation for the basal Datangpo shale in Nanhua Basin. The ratio of $Fe_{HR}/Fe_T > 0.38$ indicates anoxic conditions; $Fe_{Py}/Fe_{HR} > 0.7$ suggests euxinic conditions and $Fe_{Py}/Fe_{HR} < 0.7$ suggests ferruginous conditions (Raiswell et al., 2018).

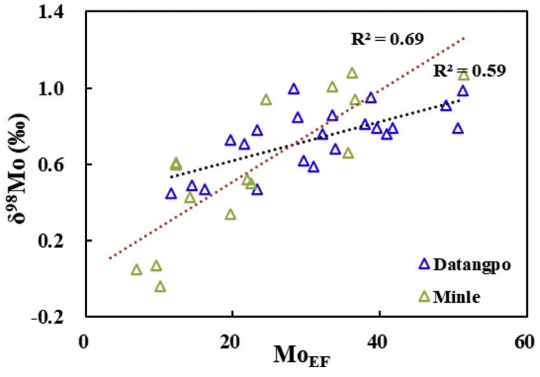


**Fig. 10.** Relationships between $\delta^{98}Mo$ and $Mo_{EF}$. Minle data are from Cheng et al., (2018); Datangpo data are from this study.

magnitudes of Mo isotopic fractionation (Fig. 11b). Relative to the contemporaneous euxinic black shales, the Datangpo Mn carbonates (with the two outliers excluded) were depleted in $^{98}Mo$ by up to 1.03‰ (relative to the heaviest value +1.1‰ by Cheng et al. (2018)). The queluzite Mn-ore were depleted in $^{98}Mo$ as large as 2.6‰ relative to their hosted graphitic schist (with the heaviest value +0.8‰). The modern Baltic sapropels were depleted in $^{98}Mo$ even up to 3.0‰ relative to modern ocean water. Therefore, the Datangpo Mn carbonates are distinct from the other Mn-enriched units by Mo depletion and a relatively small Mo isotopic fractionation.

Though large Mo enrichment and isotopic fractionation exist for both The Morro da Mina Mn-ore samples and modern Baltic sapropels, different explanations have been suggested, which are related to not only the redox characteristics (euxinic, anoxic, or suboxic) but also the depositional models of Mn carbonate (direct or two-steps). In the modern marine environment, the lighter Mo isotopes could be delivered to sediments by: (1) the shuttling of Mn oxides (Scholz et al., 2013, 2018) and (2) the incomplete conversion of molybdates to tetrathiomolybdates (Tossell, 2005; Neubert et al., 2008) under weakly sulfidic

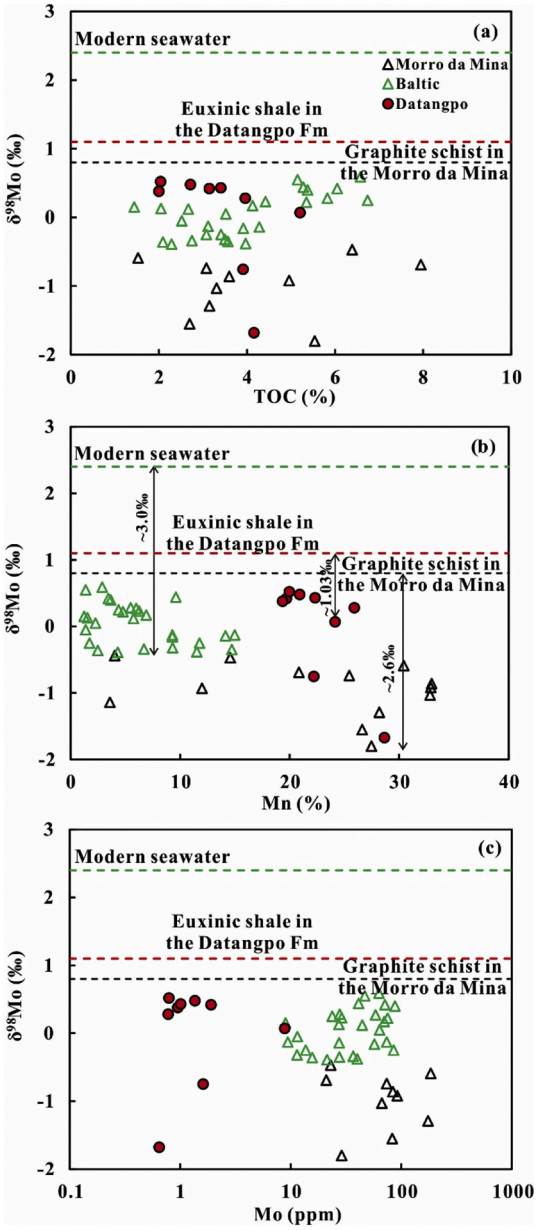


**Fig. 11.** The cross plots of $\delta^{98}$Mo and TOC with Mn and Mo contents in Mn-rich sediments, including Paleoproterozoic Morro da Mina Mn-ore deposits, modern Baltic sapropel sediments, and the Datangpo Mn carbomate. The $\delta^{98}$Mo value of Modern seawater is 2.3‰ (Siebert et al., 2003). The maximum $\delta^{98}$Mo value of euxinic shale in the Datangpo Formation is 1.08‰ from Cheng et al. (2018). The maximum $\delta^{98}$Mo value of the graphite schist is 0.8‰ in the Morro da Mina Mn-ore deposit from Cabral et al. (2019).

conditions.

Model 1 Mn oxide shuttle and direct Mn carbonate precipitation in euxinic conditions. This case is best shown by the Paleoproterozoic Morro da Mina queluzite hosted by OM-enriched greenschist (Fig. 12a). The extremely large Mo isotopic fractionation (up to 2.6‰) was suggested to be indicative of the signal of preexisting Mn oxides, and a strongly sulfidic bottom water can be inferred by common presence of molybdenite. Thus, a stratified water column was established during the deposition of queluzite. A large amount of dissolved $Mn^{2+}$, brought to the slope facies from the deep water through upwelling, was first oxidized to Mn oxides within the surface water. When the Mn-oxide particles that have adsorbed abundant light Mo sunk into a lower euxinic water body, they were again dissolved into $Mn^{2+}$, and released Mo (light isotopes) were largely captured by OM or pyrite under sulfidic conditions. The dissolved $Mn^{2+}$ were precipitated as Mn carbonates and other silicate-associated Mn-bearing minerals upon optimal conditions during burial in carbonaceous sediment. The precipitation of Mn carbonate may be not necessarily through the diagenetic reduction of Mn oxides at water-sediment interface or within the uppermost part of the sediments, and therefore can be termed as a "direct precipitation", as shown by what occurs in modern euxinic lakes (Wittkop et al., 2020).

Model 2 includes Mn oxide shuttling and diagenetic Mn carbonate formation during episodic bottom water oxygenation (Fig. 12b). Strong Mn enrichment (up to 32%) has been found to be commonly associated with the periods of bottom water oxygenation (Häusler et al., 2018), caused by major Baltic inflows and medium-intensity inflow events (Huckriede and Meischner, 1996; Burchard et al., 2005). Therefore, a first formation of Mn oxides at the water-sediment interface and subsequent diagenetic reduction into Mn carbonates within reducing sediments resulted in large Mn accumulation in the sediments. This model is emphasized by many studies for the Mn carbonates hosted by carbonaceous sediments, which were deposited in deep-water facies and well below the chemocline (Calvert and Pedersen, 1996; Huckriede and Meischner, 1996; Polgári et al., 2012). The light Mo isotope enrichment in the sediments could be explained by the capture of a large amount of light Mo absorbed by Mn oxides (Hardisty et al., 2016). After burial of Mn oxides into the sediments, they were reduced and dissolved, and the released light Mo was captured by abundant OM or pyrite in sulfidic pore water (Scholz et al., 2018). In addition, molybdate conversion to tetrathiomolybdate was incomplete under weakly euxinic conditions, which can also lead to greatly enriched light Mo (Hardisty et al., 2016). For example, large isotopic offsets of up to ~3‰ lower than seawater are observed in the Black Sea sediments deposited near the chemocline ($[H_2S]_{aq} < 11$uM; Neubert et al., 2008). Therefore, these two factors could have contributed to the formation of Mn-enriched sapropels with Mo enrichment and negative Mo isotope values (Hardisty et al., 2016).

The PAAS-normalized REE patterns of the Datangpo Mn carbonate show no marked fractionations between light REEs, heavy REEs, and consistently positive Ce, which are typical of modern marine ferromanganese oxide precipitates (Fig. 5; Bau et al., 2014; Xiao et al., 2017). Similar to Mn carbonate in the Baltic Sea, the Datangpo Mn deposits with $^{13}$C-depleted isotopes form in the deep basin floor. Therefore, Yu et al. (2016, 2017) inferred that the "episodic ventilation" model could be applied to explain the formation of Mn oxides in sediment-water interface. After co-burial with organic-rich sediments, Mn-oxides were reduced during organic matter oxidation, which led to the formation of secondary Mn-carbonates (Fig. 12c).

The low Mo concentration and moderately $\delta^{98}$Mo-depleted characteristics in the Datangpo Mn carbonates were attributed to Mo release after Mn oxides reduction in non-euxinic sediments (Fig. 12c). The pore water could have been anoxic (not sulfidic) or suboxic, and the released Mo was not fixed within the sediments and thus diffused back into water column (Scholz et al., 2011; Kurzweil et al., 2016). It has been reported that even though the dissolved $H_2S$ in pore water is low, Mo burial fluxes to sediments are ~2–3 orders of magnitude higher than oxic bottom water (Scott et al., 2008; Poulson Brucker et al., 2009). If a weakly euxinic condition was kept in the pore water, then the Mo content in Mn carbonates may be not much lower than that in black shales. Besides oxidizing OM ($CH_2O + 2MnO_2 + 2H^+ = CO_3^{2-} + 2Mn^{2+} + 2H_2O$), the Mn oxides also reacted with sulfides and dissolved $H_2S$, e.g. $H_2S + 4MnO_2 + 2H_2O = SO_4^{2-} + 4Mn^{2+} + 6OH^-$. This reaction would greatly consume the sulfides and dissolve $H_2S$. Moreover, relatively low sulfate input into Nahua Basin during the interglacial period, inferred by ultra-heavy pyrite sulfur isotopes (Chen et al., 2008; Li et al., 2012), may be an important factor leading to the less $H_2S$ conditions. Since most Mo has diffused back into the water column, the light Mo isotopic signatures absorbed by Mn-oxides may not necessarily be captured by sediments. Therefore, most Mn carbonates are not extremely depleted in $^{98}$Mo like those in reported data (Hardisty et al., 2016; Cabral et al., 2019).

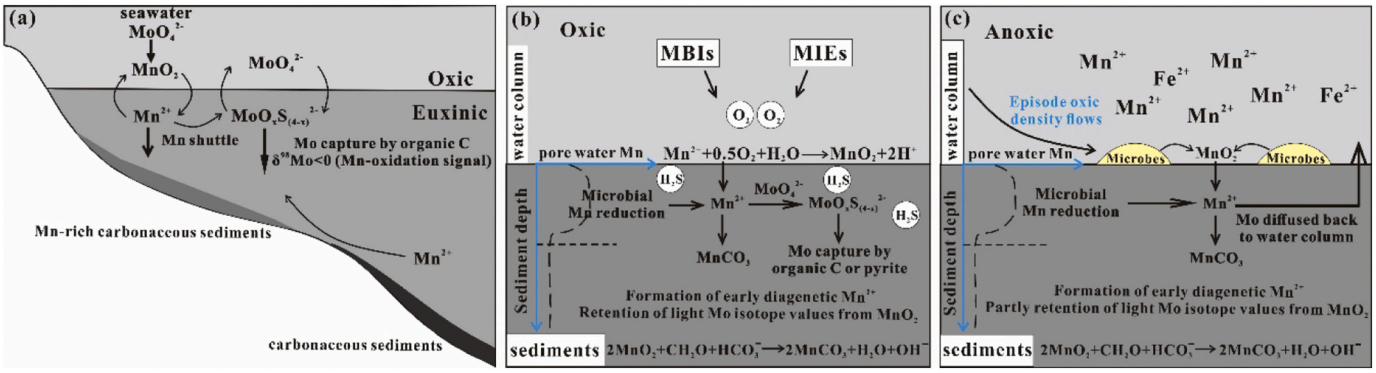


**Fig. 12.** Formation models for manganiferous sediments and the Mo cycle in the (a) Morro da Mina, (b) Baltic sediments, and (c) Datangpo Mn carbonates. (a) Direct precipitation model for Mn-rich carbonaceous sediments at Morro da Mina, modified from Cabral et al. (2019). (b) Diagenetic model for manganiferous sediments at the Baltic sea, modified from Huckriede and Meischner (1996), Hardisty et al. (2016), and Häusler et al. (2018).

### 5.3. OM accumulation mechanisms in the basal Datangpo Formation

Common high TOC content within black shale is associated with increased nutrient fluxes to the ocean as a result of enhanced chemical weathering under a relatively warm climate and high atmospheric $CO_2$ level (Hoffman et al., 1998; Planavsky et al., 2010; Mills et al., 2011; Wei et al., 2020). In this scenario, high primary productivity and euxinic water body could have been triggered within a rift-type basin like the Nanhua Basin with restriction to the open sea depending on the sea level (Fig. 13a, Li et al., 2012; Cheng et al., 2018). In return, multiple OM would be preserved through the formation of high-molecular-weight OM (vulcanization) resulting from the incorporation of inorganic sulfur into low-molecular-weight lipids under a sulfidic environment (Sinninghe Damsté et al., 1989). Additionally, the Cyclostratigraphic study of one typical drill core for the whole Datangpo Formation has revealed a duration of 1.3 Myr for the deposition of the black shale member (Bao et al., 2018), based on which a linear sedimentation rate of ~2.5 cm/kyr can be obtained. This sedimentation rate may be also good

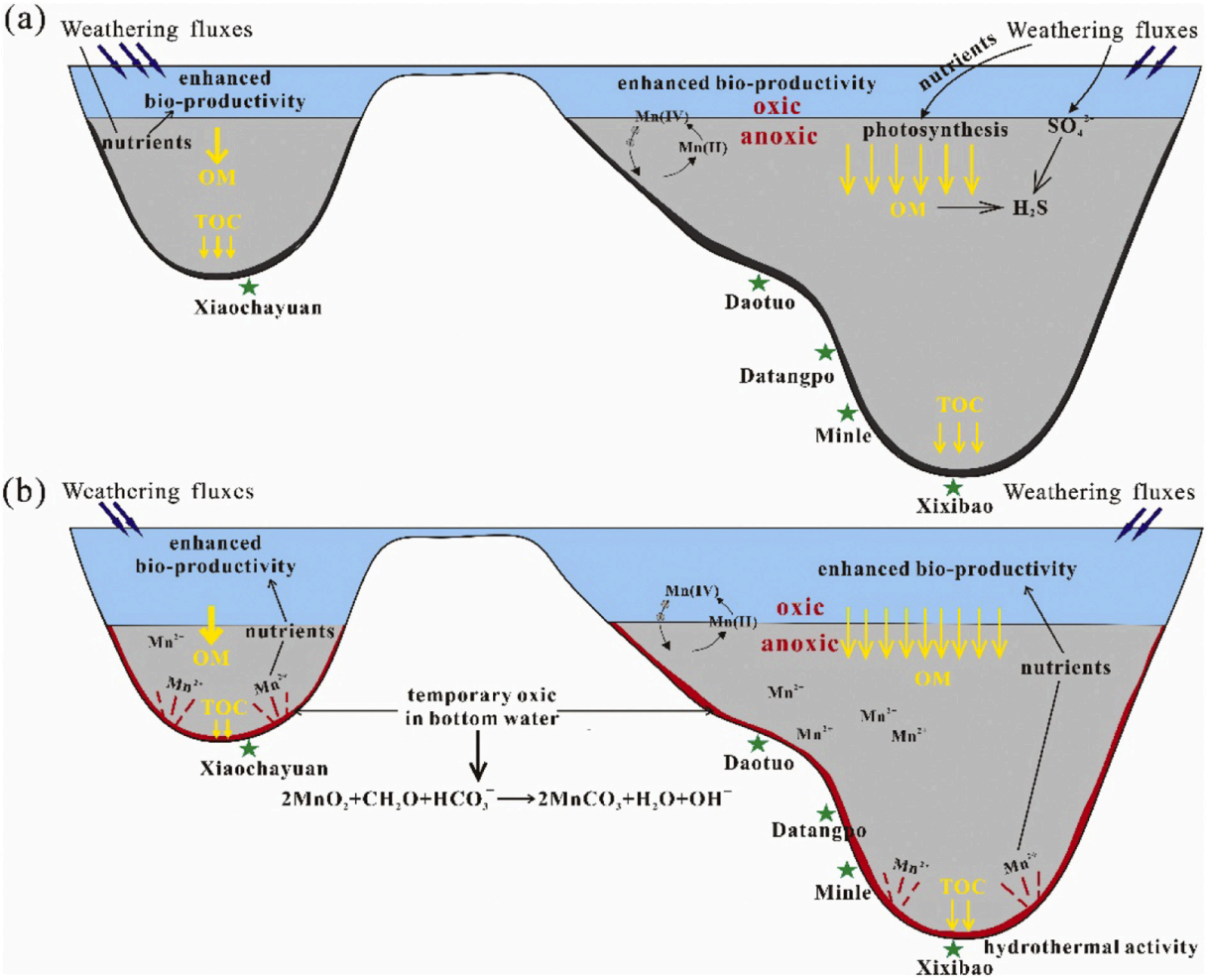


**Fig. 13.** Depositional model showing OM enrichment mechanisms in (a) black shale and (b) Mn carbonate intervals.

for the OM accumulation (Tyson, 2001).

Episodic bottom water oxygenation and OM oxidation accompanied by the diagenetic reduction of Mn oxides within sediments (see Section 5.2) are both unfavorable for OM preservation during the period of Mn carbonate deposition. Published data were compiled with the present results and are shown in Fig. 14. The TOC content of black shales (mostly with Mn <1%) varies greatly but shows no relationship with Mn content (Fig. 14a). With increasing Mn enrichment, the TOC content in the Mn shales (10% > Mn > 1%) progressively decreases (Fig. 14a). The average TOC content of black shales (Mn < 1%) is 3.31% ($n$ = 86), notably higher than that of Mn shales (average 2.46%, $n$ = 25) and Mn carbonate (average 2.45%, $n$ = 58) (Fig. 14b). These results indicate a predominance of OM consumption or degradation within the Mn-rich interval.

However, one should note that the formation of a large amount of Mn carbonate (Mn > 10%) has not caused the OM content to be significantly lower than the Mn shale sample (Fig. 14b). In contrast, the co-variation of Mn and TOC contents shown by the Mn carbonates in our study section (Fig. 3) calls for other factors to be responsible for this phenomenon.

Both OM and Mn enrichment could be mainly attributed to the high primary productivity caused by submarine hydrothermal activity introducing abundant nutrients (Figs. 6, 7). In the modern hydrothermally active Fiji basin, higher intensity of biological activity, 1–3 orders of magnitude higher than the ordinary modern ocean, are associated with the area closer to the hydrothermal source (Halbach et al., 2001). The hydrothermal contribution could represent up to 25% of the global deep ocean organic carbon inventory (Maruyama et al., 1998). In the ancient ocean, hydrothermally released Fe during the Paleoproterozoic deglaciation could trigger a phytoplankton bloom, possibly including cyanobacteria (Kirschvink et al., 2000). Compiled data from multiple sections in the Nanhua Basin show that a slight positive correlation could be observed between TOC and Mn content (from 10% up to 30%, Fig. 14a), suggesting a predominance of OM input over depletion during this stage of Mn carbonate formation. Therefore, the statistical results support the covariation of TOC and Mn contents elucidated in the individual sections of this study (Fig. 3). In addition to enhanced primary productivity and OM input, the OM preservation also benefits from the enhanced microbe activity. For example, $Mn^{2+}$ oxidation mediated by Mn-oxidizing microbes has been suggested to occur within the extracellular polymeric substances (EPS) of the cyanobacteria organic network (Yu et al., 2019). These EPS are resistant to chemical or microbial degradation and thought to be an important contributor to OM preservation in ancient sediments (Pacton et al., 2007). In combination, both OM and Mn enrichment could be associated with enhanced microbes and bacteria activity, fueled by the hydrothermal fluids and their contained nutrients as shown by the Datangpo Mn carbonates (Fig. 13b).

### 5.4. Implications for redox conditions during the Cryogenian interglacial

The isotopic composition and abundance of seawater Mo provide information about the global ocean redox state. In the modern ocean, widespread oxygenation supports large seawater reservoirs of Mo, which enables strong sedimentary Mo accumulation in the anoxic organic-rich marine sediments that cover a small percentage of the ocean floor (Scott et al., 2008). Furthermore, the preferential adsorption of light Mo isotopes onto the Mn oxides beneath oxygenated waters results in heavy Mo isotopic composition in global seawater today ($\delta^{98}$Mo = 2.34 ± 0.10‰, Barling et al., 2001, Siebert et al., 2003). Therefore, high abundances and $\delta^{98}$Mo values are observed in widely oxic oceans, whereas low concentrations and light Mo occurred in a pervasively anoxic one (Scott et al., 2008; Dahl et al., 2010). In a strong euxinic basin, sediments have the potential to capture a seawater-like $\delta^{98}$Mo signature and constrain the oxygenation state of the global ocean due to a small isotopic offset between seawater and sediments $\delta^{98}$Mo ($\Delta^{98}$Mo ≤ 0.5 ± 0.3% Barling et al., 2001; Neubert et al., 2008). Here, the highest $\delta^{98}$Mo from each interval could be used as a minimum estimate of seawater $\delta^{98}$Mo (Dahl et al., 2010).

Low Mo concentrations and $\delta^{98}$Mo values during interglaciation indicate a global ocean with extensive anoxic conditions occurring after the Sturtian glaciation (Fig. 15, Cheng et al., 2018; Scheller et al., 2018). These interglacial strata show similar low Mo concentrations, including the Datangpo Fm, the MacDonaldryggen Member, the Arean Fm, and the Twitya Fm (Li et al., 2012, Ye et al., 2018; Ma et al., 2019; Kunzmann et al., 2015; Sperling et al., 2016; Scheller et al., 2018 and this study), which imply that a low Mo reservoir is a characteristic feature of the global ocean during the Cryogenian. The Datangpo Fm contains the highest $\delta^{98}$Mo value of~1.1‰ (Cheng et al., 2018), while the contemporaneous Arean Fm displays a maximal $\delta^{98}$Mo value at ~1.5‰ (Scheller et al., 2018). Hence, the best estimates of Cryogenian ocean $\delta^{98}$Mo values vary between 1.1‰ and 1.5‰. According to an isotopic mass-balance model, euxinic conditions covering 0.1–1.0% of the seafloor would lead to oceanic $\delta^{98}$Mo of 1.1–1.5‰ and 3–6-fold lower Mo concentrations than the modern ocean (Dahl et al., 2011). Similar to the ocean state at ~750 Ma, this is a 2–20 fold greater extent of euxinic seafloor area than modern oceans (Dahl et al., 2011). Still, anoxic and ferruginous conditions were likely even more pervasive in the deep

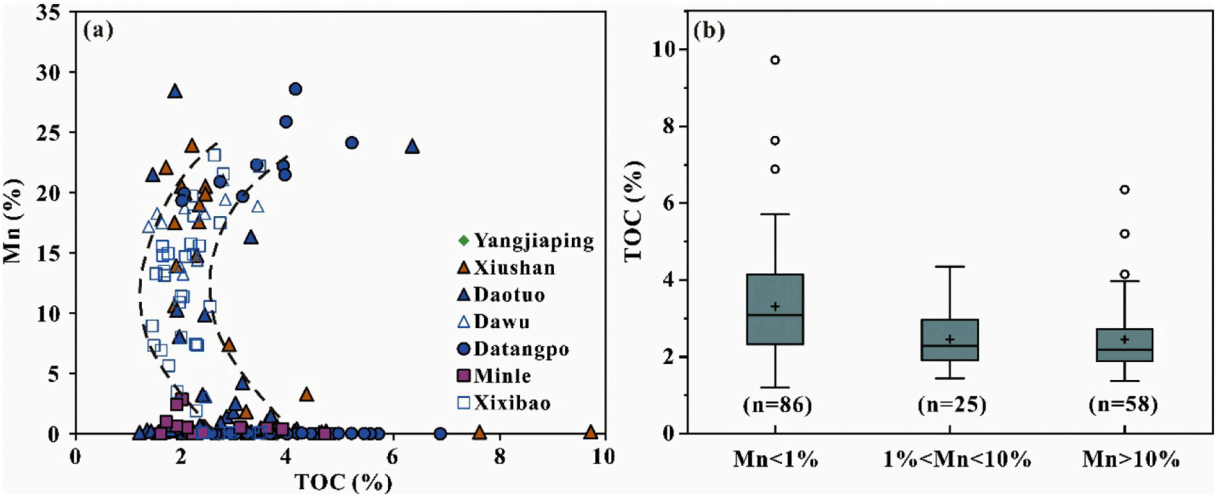


**Fig. 14.** (a) Cross plots of Mn versus TOC for samples from the different sections in Nanhua Basin. (b) Whisker plots showing TOC content in the Datangpo Formation from different Mn contents. Xiushan data are from Wu et al., 2016 and Ma et al., 2019, Daotuo data are from Zhang et al., 2015 and Ye et al., 2018, Datangpo data are from this study, Minle data are from Li et al., 2012, and Xixibao data are fm Yu et al., 2016.

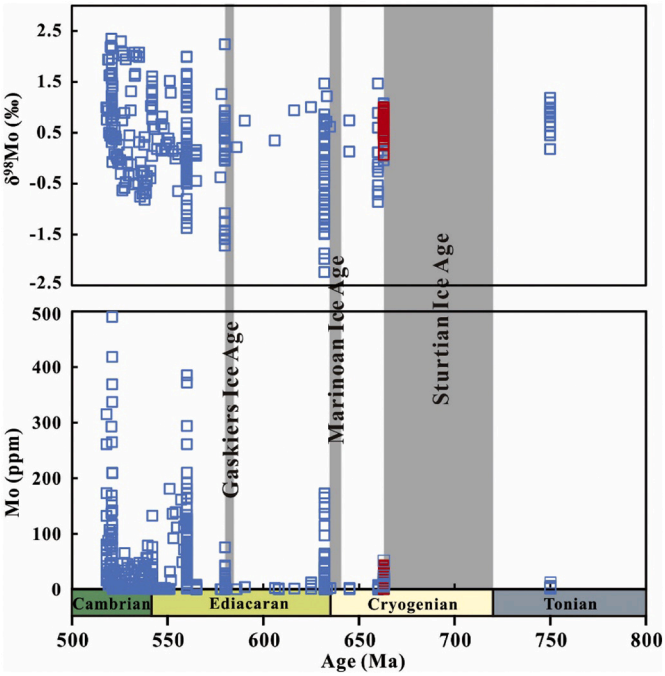


**Fig. 15.** Mo concentrations and Mo isotopes of sedimentary rocks deposited during 750–510 Ma. Mo concentration data sources: Jiang et al. (2006), Lehmann et al. (2007), Wille et al. (2008), Zhou and Jiang (2009), Yu et al. (2009), Li et al. (2010), Dahl et al. (2010), Wen et al. (2011), Sahoo et al. (2012, 2016), Xu et al. (2013), Chen et al. (2015), Kendall et al. (2006, 2015), Dahl et al. (2010, 2011), Cheng et al. (2018), Scheller et al. (2018), Ostrander et al. (2019) and this study (red squares); $\delta^{98}$Mo data sources: Kendall et al. (2006, 2015), Lehmann et al. (2007), Wille et al. (2008), Dahl et al. (2010, 2011), Wen et al. (2011), Xu et al. (2013), Chen et al. (2015), Cheng et al. (2018), Scheller et al. (2018), Ostrander et al. (2019), and this study (red squares). (For interpretation of the references to colour in this figure legend, the reader is referred to the web version of this article.)

ocean (Canfield et al., 2008; Li et al., 2012).

An interval of low $\delta^{98}$Mo and little Mo reservoir between ~750 Ma and ~635 Ma (Fig. 15) points to a persistently anoxic pre-Ediacaran ocean. Based on high enrichments of Mo and U for Member II of the Doushantuo Formation, however, Sahoo et al. (2012) argued oxygen buildup beginning only at the early Ediacaran. Furthermore, Kendall et al. (2015) reported high $\delta^{98}$Mo and $\delta^{238}$U values for Member IV (~560 Ma) of the Doushantuo Formation, showing a widely oxidized ocean. A recent model provided by Reinhard et al. (2016b) showed that dissolved oxygen concentrations in the ocean are largely constrained by marine productivity under low atmospheric oxygen levels (< 2.5% PAL). This inference may be supported by evidence of the compilation and biogeochemical modeling of global P data (Reinhard et al., 2016a). More specifically, high dissolved P concentrations enhanced oceanic productivity and organic carbon burial, finally promoting more oxidizing conditions in the Ediacaran oceans. Therefore, we infer that Neoproterozoic ocean oxygenation was postponed to the Ediacaran, rather than the Cryogenian.

## 6. Conclusions

Geochemical and Mo isotopic compositions have been analyzed and compared for the Mn carbonates and black shales from a new section of the OM-rich basal Datangpo Formation in the Nanhua Basin. The redox conditions and controlling factors on OM accumulation in the basal formation were explored after compiling the data, and three main conclusions obtained are:

(1) Different from typical ancient and modern Mn ore analogs, the Datangpo Mn carbonates are characterized by very low Mo content and slightly light Mo isotopic composition, suggesting different scenarios for the Mo behaviors during the Mn ore formation. Constrained by the diagenetic reduction of Mn oxides that formed during episodic deep-water ventilations, the Datangpo Mn carbonate developed in suboxic or anoxic (non-sulfide) pore waters inferred from the Mo content and isotopes. During the reduction (dissolution) of Mn oxides, Mo once absorbed onto Mn oxides were released and then diffused back to the water column again, resulting in low Mo content in the Mn carbonates. This significant desorption and subsequent diffusion process may also cause very few opportunities for the capture of large amounts of the light Mo isotope that had been preferentially adsorbed by Mn oxides.

(2) The Mn carbonate formation is usually accompanied by the remineralization of sedimentary OM, which would lower the OM content. However, a close relationship between OM enrichment and Mn ore formation can be indicated by the co-varied Mn, TOC, and TIC contents in the Mn carbonates of this study, as well as the slightly increased TOC content with Mn content higher than 10% from a large compiling dataset. This result was mainly attributed to the higher nutrient input associated with hydrothermal activity and enhanced primary productivity during the Mn deposition period.

(3) The combination of low Mo concentration and $\delta^{98}$Mo values in euxinic shales suggests that widespread anoxia prevailed during the Cryogenian interglaciation. In contrast, a compilation of Mo isotope data suggests that Neoproterozoic oceanic oxygenation likely first developed in the Ediacaran rather than the Cryogenian.

## Declaration of Competing Interest

None.

## Acknowledgements

This study was financially supported by the National Key Research and Development Program of China (2017YFC0603101), National Oil and Gas Major Project (2017ZX05008-002-010), the “135” Project of GIG-CAS (135TP201602), and State Key Laboratory of Organic Geochemistry (SKLOG2016-A01). We thank Dr. Xi Chen for the helpful discussions and constructive suggestions.

## Appendix A. Supplementary data

Supplementary data to this article can be found online at https://doi.org/10.1016/j.palaeo.2020.110169.

## References

Algeo, T.J., Liu, J.S., 2020. A re-assessment of elemental proxies for paleoredox analysis. Chem. Geol. 540.
Algeo, T.J., Lyons, T.W., 2006. Mo-total organic carbon covariation in modern anoxic marine environments: implications for analysis of paleoredox and paleohydrographic conditions. Paleoceanography 21. PA1016 23 pp.
Archer, C., Vance, D., 2008. The isotopic signature of the global riverine molybdenum flux and anoxia in the ancient oceans. Nat. Geosci. 1, 597–600.
Bao, X., Zhang, S., Jiang, G., Wu, H., Li, H., Wang, X., et al., 2018. Cyclostratigraphic constraints on the duration of the Datangpo Formation and the onset age of the Nantuo (Marinoan) glaciation in South China. Earth Planet. Sci. Lett. 483, 52–63.
Barling, J., Arnold, G.L., Anbar, A.D., 2001. Natural mass-dependent variations in the isotopic composition of molybdenum. Earth Planet Sci. Lett. 193, 447–457.
Batumike, M.J., Cailteux, J.L.H., Kampunzu, A.B., 2007. Lithostratigraphy, basin development, base metal deposits, and regional correlations of the Neoproterozoic Nguba and Kundelungu rock successions, central African Copperbelt. Gondwana Res. 11, 432–447.

Bau, M., Schmidt, K., Koschinsky, A., Hein, J., Kuhn, T., Usui, A., 2014. Discriminating between different genetic types of marine ferro-manganese crusts and nodules based on rare earth elements and yttrium. Chem. Geol. 381, 1–9.
Boström, K., 1983. Genesis of ferromanganese deposits—diagnostic criteria for recent and old deposits. In: Rona, P.A. (Ed.), Hydrothermal Processes at Seafloor Spreading Centers. Springer, Berlin, pp. 473–489.
Burchard, H., Lass, H.U., Mohrholz, V., Umlauf, L., Sellschopp, J., Fiekas, V., Bolding, K., Arneborg, L., 2005. Dynamics of medium-intensity dense water plumes in the Arkona Basin, western Baltic Sea. Ocean Dyn. 55, 391–402.
Cabral, A.R., Zeh, A., Vianna, N.C., Ackerman, L., Pašava, J., Bernd Lehmann, B., Chrastný, V., 2019. Molybdenum-isotope signals and cerium anomalies in Palaeoproterozoic manganese ore survive high-grade metamorphism. Sci. Rep. 9, 4570.
Calvert, S.E., Pedersen, T.F., 1996. Sedimentary geochemistry of manganese; implications for the environment of formation of manganiferous black shales. Econ. Geol. 91, 36–47.
Canfield, D.E., Poulton, S.W., Knoll, A.H., Narbonne, G.M., Ross, G., Goldberg, T., Strauss, H., 2008. Ferruginous conditions dominated later neoproterozoic deep-water chemistry. Science. 321, 949–952.
Chen, X., Li, D., Ling, H.F., Jiang, S.Y., 2008. Carbon and sulfur isotopic compositions of basal Datangpo Formation, northeastern Guizhou, South China: implications for depositional environment. Prog. Nat. Sci. 18, 421–429.
Chen, X., Ling, H.F., Vance, D., Shields-Zhou, G.A., Zhu, M., Poulton, S.W., Och, L.M., Jiang, S.Y., Li, D., Cremonese, L., Archer, C., 2015. Rise to modern levels of ocean oxygenation coincided with the Cambrian radiation of animals. Nat. Commun. 6, 7.
Cheng, M., Li, C., Chen, X., Zhou, L., Algeo, T.J., Ling, H.F., Feng, L.J., Jin, C.S., 2018. Delayed Neoproterozoic oceanic oxygenation: evidence from Mo isotopes of the Cryogenian Datangpo Formation. Precambrian Res. 319, 187–197.
Dahl, T.W., Hammarlund, E.U., Anbar, A.D., Bond, D.P.G., Gill, B.C., Gordon, G.W., Knoll, A.H., Nielsen, A.T., Schovsbo, N.H., Canfield, D.E., 2010. Devonian rise in atmospheric oxygen correlated to the radiations of terrestrial plants and large predatory fish. Proc. Natl. Acad. Sci. U. S. A. 107, 17911–17915.
Dahl, T.W., Canfield, D.E., Rosing, M.T., Frei, R.E., Gordon, G.W., Knoll, A.H., Anbar, A. D., 2011. Molybdenum evidence for expansive sulfidic water masses in ~750Ma oceans. Earth Planet. Sci. Lett. 311, 264–274.
Dahl, T.W., Chappaz, A., Fitts, J.P., Lyons, T.W., 2013. Molybdenum reduction in a sulfidic lake: evidence from X-ray absorption fine-structure spectroscopy and implications for the Mo paleoproxy. Geochim. Cosmochim. Acta 2013 (103), 213–231.
Dick, G.J., Anantharaman, K., Baker, B.J., Li, M., Reed, D.C., Sheik, C.S., 2013. The microbiology of deep-sea hydrothermal vent plumes: ecological and biogeographic linkages to seafloor and water column habitats. Front. Microbiol. 4, 124.
Donnadieu, Y., Goddéris, Yves, Ramstein, G., Nédélec, A., Meert, J., 2004. A 'snowball Earth' climate triggered by continental break-up through changes in runoff. Nature 428, 303–306.
Halbach, P., Holzbecher, E., Koschinsky, A., Michaelis, W., Seifert, R., 2001. Deep sea hydrothermal microplume generation—a case study from the North Fiji Basin. Geo-Mar. Lett. 21, 94–102.
Hardisty, D.S., Riedinger, N., Planavsky, N.J., Asael, D., Andrén, T., Jørgensen, B.B., Lyons, T.W., 2016. A Holocene history of dynamic water column redox conditions in the Landsort deep, Baltic Sea. Am. J. Sci. 316, 713–745.
Häusler, K., Dellwiga, O., Schnetger, B., Feldens, P., Leipe, T., Moros, M., Pollehne, F., Schönke, M., Wegwerth, A., Arz, H.W., 2018. Massive Mn carbonate formation in the Landsort Deep (Baltic Sea): hydrographic conditions, temporal succession, and Mn budget calculations. Mar. Geol. 395, 260–270.
Helz, G.R., Miller, C.V., Charnock, J.M., Mosselmans, J.F.W., Pattrick, R.A.D., Garner, C. D., Vaughan, D.J., 1996. Mechanism of molybdenum removal from the sea and its concentration in black shales: EXAFS evidence. Geochim. Cosmochim. Acta 60, 3631–3642.
Helz, G.R., Bura-Nakić, E., Mikac, N., 2011. New model for molybdenum behavior in euxinic waters. Chem. Geol. 284, 323–332.
Hoffman, P.F., Kaufman, A.J., Halverson, G.P., Schrag, D.P., 1998. A Neoproterozoic snowball earth. Science 281, 1342.
Hoffman, P.F., Abbot, D.S., Ashkenazy, Y., Benn, D.I., Brocks, J.J., Cohen, P.A., Cox, G. M., Creveling, J.R., Donnadieu, Y., Erwin, D.H., Fairchild, I.J., Ferreira, D., Goodman, J.C., Halverson, G.P., Jansen, M.F., Le Hir, G., Love, G.D., Macdonald, F. A., Maloof, A.C., Partin, C.A., Ramstein, G., Rose, B.E.J., Rose, C.V., Sadler, P.M., Tziperman, E., Voigt, A., Warren, S.G., 2017. Snowball Earth climate dynamics and Cryogenian geology-geobiology. Sci. Adv. 3, 1–43.
Huckriede, H., Meischner, D., 1996. Origin and environment ofmanganese-rich sediments within black-shale basins. Geochim. Cosmochim. Acta 60, 1399–1413.
Hung, J.J., Yeh, H.Y., Peng, S.H., Chen, C.T.A., 2018. Influence of submarine hydrothermalism on sulfur and metal accumulation in surface sediments in the Kueishantao venting field off northeastern Taiwan. Mar. Chem. 198, 88–96.
Jiang, S.Y., Chen, Y.Q., Ling, H.F., Yang, J.H., 2006. Trace- and rare-earth element geochemistry and Pb–Pb dating of black shales and intercalated Ni–Mo–PGE–Au sulfide ores in Lower Cambrian strata, Yangtze Platform, South China. Mineral. Deposita 41, 453–467.
Jiang, G.Q., Shi, X.Y., Zhang, S.H., Wang, Y., Xiao, S.H., 2011. Stratigraphy and paleogeography of the Ediacaran Doushantuo formation (ca. 635–551 Ma) in south China. Gondwana Res. 19, 831–849.
Kendall, B., Creaser, R.A., Selby, D., 2006. Re-Os geochronology of postglacial black shales in Australia: constraints on the timing of "sturtian" glaciation. Geology 34, 729–732.
Kendall, B., Komiya, T., Lyons, T.W., Bates, S.M., Gordon, G.W., Romaniello, S.J., Jiang, G., Creaser, R.A., Xiao, S., McFadden, K., Sawaki, Y., Tahata, M., Shu, D., Han, J., Li, Y., Chu, X., Anbar, A.D., 2015. Uranium and molybdenum isotope evidence for an episode of widespread ocean oxygenation during the late Ediacaran Period. Geochim. Cosmochim. Acta 156, 173–193.
Kirschvink, J.L., Gaidos, E.J., Elizabeth Bertani, L., Beukes, N.J., Gutzmer, J., Maepa, L. N., Steinberger, R.E., 2000. Paleoproterozoic snowball earth: extreme climatic and geochemical global change and its biological consequences. Proc. Natl. Acad. Sci. U. S. A. 97, 1400–1405.
Kunzmann, M., Halverson, G.P., Scott, C., Minarik, W.G., Wing, B.A., 2015. Geochemistry of Neoproterozoic black shales from Svalbard: Implications for oceanic redox conditions spanning Cryogenian glaciations. Chem. Geol. 417, 383–393.
Kurzweil, F., Wille, M., Gantert, N., Beukes, N.J., Schoenberg, R., 2016. Manganese oxide shuttling in pre-GOE oceans–evidence from molybdenum and iron isotopes. Earth Planet. Sci. Lett. 452, 69–78.
Lau, K.V., Macdonald, F.A., Maher, K., Payne, J.L., 2017. Uranium isotope evidence for temporary ocean oxygenation in the aftermath of the Sturtian Snowball Earth. Earth Planet. Sci. Lett. 458, 282–292.
Laurila, T.E., Hannington, M.D., Leybourne, M., Petersen, S., Devey, C.W., Garbe-Schönberg, D., 2015. New insights into the mineralogy of the Atlantis II deep metalliferous sediments, Red Sea. Geochem. Geophys. Geosyst. 16, 4449–4478.
Lehmann, B., Nägler, T.F., Wille, M., Holland, H.D., Mao, J., 2007. Highly metalliferous carbonaceous shale and Early Cambrian seawater. Geology 35, 403–406.
Li, C., Love, G.D., Lyons, T.W., Scott, C.T., Feng, L., Huang, J., Chang, H., Zhang, Q., Chu, X., 2012. Evidence for a redox stratified Cryogenian marine basin, Datangpo Formation, South China. Earth Planet. Sci. Lett. 331–332, 246–256.
Li, Z.X., Evans, D.A.D., Halverson, G.P., 2013. Neoproterozoic glaciations in a revised global palaeogeography from the breakup of Rodinia to the assembly of Gondwanaland. Sediment. Geol. 294, 219–232.
Li, J., Liang, X.R., Zhong, L.F., Wang, X.C., Ren, Z.Y., Sun, S.L., Zhang, Z.F., Xu, J.F., 2014. Measurement of the isotopic composition of molybdenum in geological samples by MC-ICP-MS using a novel chromatographic extraction technique. Geostand. Geoanal. Res. 38, 345–354.
Li, C., Love, G.D., Lyons, T.W., Fike, D.A., Sessions, A.L., Chu, X.L., 2010. A stratified redox model for the ediacaran ocean. Science 328, 80–83.
Ma, Z., Liu, X., Yu, W., Du, Y., Du, Q., 2019. Redox conditions and manganese metallogenesis in the Cryogenian Nanhua Basin: Insight from the basal Datangpo Formation of South China. Palaeogeogr. Palaeoclimatol. Palaeoecol. 529, 39–52.
Marchig, V., Gundlach, H., Möller, P., Schley, F., 1982. Some geochemical indicators for discrimination between diagenetic and hydrothermal metalliferous sediments. Mar. Geol. 50, 241–256.
Maruyama, A., Urabe, T., Ishibashi, J., Feely, R.A., Baker, E.T., 1998. Global hydrothermal primary production rate estimated from the southern East Pacific Rise. Cah. Biol. Mar. 39, 249–252.
Maynard, J.B., 2014. Manganiferous sediments, rocks, and ores. In: MacKenzie, F.T. (Ed.), Treatise of Geochemistry, Sediments, Diagenesis, and Sedimentary Rocks, 2nd edition, 9. Elsevier, Amsterdam, pp. 327–349.
McKirdy, D.M., Burgess, J.M., Lemon, N.M., Yu, X.K., Cooper, A.M., Gostin, V.A., Jenkins, R.J.F., Both, R.A., 2001. A chemostratigraphic overview of the late Cryogenian interglacial sequence in the Adelaide Fold-Thrust Belt, South Australia. Precambrian Res. 106, 149–186.
McLennan, S.M., 1993. Weathering and global denudation. J. Geol. 101, 295–303.
Mills, B., Watson, A.J., Goldblatt, C., Boyle, R., Lenton, T.M., 2011. Timing of Neoproterozoic glaciations linked to transport-limited global weathering. Nat. Geosci. 4, 861–864.
Nägler, T.F., Anbar, A.D., Archer, C., Goldberg, T., Gordon, G.W., Greber, N.D., Siebert, C., Sohrin, Y., Vance, D., 2014. Proposal for an international molybdenum isotope measurement standard and data representation. Geostand. Geoanal. Res. 38, 149–151.
Nesbitt, H.W., Young, G.M., 1982. Early Proterozoic climates and plate motions inferred from major element chemistry of lutites. Nature 299, 715–717.
Neubert, N., Nägler, T.F., Böttcher, M.E., 2008. Sulfidity controls molybdenum isotope fractionation into euxinic sediments: evidence from the modern Black Sea. Geology 36, 775–778.
Och, L.M., Shields-Zhou, G.A., 2012. The Neoproterozoic oxygenation event: Environmental perturbations and biogeochemical cycling. Earth-Sci. Rev. 110, 26–57.
Olcott, A.N., Sessions, A.L., Corsetti, F.A., Kaufman, A.J., Oliviera, T.F., 2005. Biomarker evidence for photosynthesis during neoproterozoic glaciation. Science 310, 471–474.
Ostrander, C.M., Sahoo, S.K., Kendall, B., Jiang, G.Q., Planavsky, N.J., Lyons, T.W., Nielsen, S.G., Owens, J.D., Gordon, G.W., Romaniello, S.J., Anbar, A.D., 2019. Multiple negative molybdenum isotope excursions in the Doushantuo Formation (South China) fingerprint complex redox-related processes in the Ediacaran Nanhua Basin. Geochim. Cosmochim. Acta 261, 191–209.
Pacton, M., Fiet, N., Gorin, G.E., 2007. Bacterial activity and preservation of sedimentary organic matter: the role of exopolymeric substances. Geomicrobiol J. 24, 571–581.
Peter, J.M., Goodfellow, W.D., 1996. Mineralogy, bulk and rare earth element geochemistry of massive sulphide-associated hydrothermal sediments of the Brunswick Horizon, Bathurst Mining Camp, New Brunswick. Can. J. Earth Sci. 33, 252–283.
Planavsky, N.J., Rouxel, O.J., Bekker, A., Lalonde, S.V., Konhauser, K.O., Reinhard, C.T., Lyons, T.W., 2010. The evolution of the marine phosphate reservoir. Nature 467, 1088–1090.
Planavsky, N.J., Mcgoldrick, P., Scott, C.T., Li, C., Reinhard, C.T., Kelly, A.E., Chu, X.L., Bekker, A., Love, G.D., Lyons, T.M., 2011. Widespread iron-rich conditions in the mid-Proterozoic ocean. Nature. 477, 448–451.

Planavsky, N.J., Asael, D., Hofmann, A., Reinhard, C.T., Lalonde, S.V., Knudsen, A., Wang, X.L., Ossa, F.O., Pecoits, E., Smith, A.J.B., Beukes, N.J., Bekker, A., Johnson, T.M., Konhauser, K.O., Lyons, T.W., Rouxel, O.J., 2014. Evidence for oxygenic photosynthesis half a billiion years before the Great Oxidation Event. Nat. Geosci. 7, 283–286.
Planavsky, N.J., Slack, J.F., Cannon, W.F., O'Connell, B., Terry-Tang, Y., Asael, D., Jackson, J.C., Hardisty, D.S., Lyons, T.W., Bekker, A., 2018. Evidence for episodic oxygenation in a weakly redox-buffered deep mid-Proterozoic ocean. Chem. Geol. 483, 581–594.
Polgári, M., Hein, J.R., Vigh, T., Szabó-Drubina, M., Fórizs, I., Bíró, L., Müller, A., Tóth, A.L., 2012. Microbial processes and the origin of the Úrkút manganese deposit, Hungary. Ore Geol. Rev. 47, 87–109.
Poulson Brucker, R.L., McManus, J., Severmann, S., Berelson, W.M., 2009. Molybdenum behavior during early diagenesis: insights from Mo isotopes. Geochem. Geophys. Geosyst. 10. Paper 2008GC002180.
Qi, L., Xu, Y., Cawood, P.A., Du, Y., 2018. Reconstructing Cryogenian to Ediacaran successions and paleogeography of the South China Block. Precambrian Res. 314, 452–467.
Raiswell, R., Hardisty, D.S., Lyons, T.W., Canfield, D.E., Owens, J.D., Planavsky, N.J., Poulton, S.W., Reinhard, C.T., 2018. The iron paleoredox proxies: a guide to the pitfalls, problems and proper practice. Am. J. Sci. 315, 491–526.
Reinhard, C.T., Planavsky, N.J., Gill, B.C., Ozaki, K., Robbins, L.J., Lyons, T.W., Fischer, W.W., Wang, C., Cole, D.B., Konhauser, K.O., 2016a. Evolution of the global phosphorus cycle. Nature 541.
Reinhard, C.T., Planavsky, N.J., Olson, S.L., Lyons, T.W., Erwin, D.H., 2016b. Earth's oxygen cycle and the evolution of animal life. Proc. Natl. Acad. Sci. U. S. A. 113.
Rieu, R., Allen, P.A., Plötze, M., Pettke, T., 2007. Climatic cycles during a Neoproterozoic "snowball" glacial epoch. Geology 35, 299–302.
Rooney, A.D., Yang, C., Condon, D.J., Zhu, M.Y., Macdonald, F.A., 2020. U-Pb and Re-Os geochronology tracks stratigraphic condensation in the Sturtian snowball Earth aftermath. Geology 48, 625–629.
Roy, S., 2006. Sedimentary manganese metallogenesis in response to the evolution of the Earth system. Earth Sci. Rev. 77, 273–305.
Sahoo, S.K., Planavsky, N.J., Kendall, B., Wang, X., Shi, X., Scott, C., Anbar, A.D., Lyons, T.W., Jiang, G., 2012. Ocean oxygenation in the wake of the Marinoan glaciation. Nature 489, 546–549.
Sahoo, S.K., Planavsky, N.J., Jiang, G., Kendall, B., Owens, J.D., Wang, X., Shi, X., Anbar, A.D., Lyons, T.W., 2016. Oceanic oxygenation events in the anoxic Ediacaran ocean. Geobiology 14, 457–468.
Scheller, E.L., Dickson, A.J., Canfield, D.E., Korte, C., Kristiansen, K.K., Dahl, T.W., 2018. Ocean redox conditions between the snowballs–Geochemical constraints from Arena Formation, East Greenland. Precambrian Res. 319, 173–186.
Schmid, S., Kunzmann, M., Pagès, A., 2018. Inorganic geochemical evaluation of hydrocarbon source rock potential of Neoproterozoic strata in the Amadeus Basin, Australia. Mar. Pet. Geol. 86, 1092–1105.
Scholz, F., Hensen, C., Noffke, A., Rohde, A., Liebetrau, V., Wallmann, K., 2011. Early diagenesis of redox-sensitive trace metals in the Peru upwelling area – response to ENSO-related oxygen fluctuations in the water column. Geochim. Cosmochim. Acta 75, 7257–7276.
Scholz, F., McManus, J., Sommer, S., 2013. The manganese and iron shuttle in a modern euxinic basin and implications for molybdenum cycling at euxinic ocean margins. Chem. Geol. 355, 56–68.
Scholz, F., Baum, M., Siebert, C., Eroglu, S., Dale, A.W., Naumann, M., Sommer, S., 2018. Sedimentary molybdenum cycling in the aftermath of seawater inflow to the intermittently euxinic Gotland Deep, Central Baltic Sea. Chem. Geol. 491, 27–38.
Scott, C., Lyons, T.W., Bekker, A., Shen, Y., Poulton, S.W., Chu, X.L., Anbar, A.D., 2008. Tracing the stepwise oxygenation of the Proterozoic ocean. Nature 452, 456–459.
Shanks, W.C.I.I.I., Bischoff, J.L., 1977. Ore transport and deposition in the Red Sea geothermal system: a geochemical model. Geochim. Cosmochim. Acta 41, 1507–1519.
Siebert, C., Nägler, T.F., Kramers, J.D., 2001. Determination of molybdenum isotope fractionation by double-spike multicollector inductively coupled plasma mass spectrometry. Geochem. Geophys. Geosyst. 2, 1032.
Siebert, C., Nägler, T.F., von Blankenburg, F., Kramers, J.D., 2003. Molybdenum isotope records as a proxy for paleoceanography. Earth Planet. Sci. Lett. 211, 159–171.
Sinninghe Damsté, J.S., Eglinton, T.I., Leeuw, J.W.D., Schenck, P.A., 1989. Organic sulphur in macromolecular sedimentary organic matter: I. Structure and origin of sulphur-containing moieties in kerogen, asphaltenes and coal as revealed by flash pyrolysis. Geochim. Cosmochim. Acta 53, 873–889.
Sperling, E.A., Carbone, C., Strauss, J.V., Johnston, D.T., Narbonne, G.M., Macdonald, F. A., 2016. Oxygen, facies, and secular controls on the appearance of Cryogenian and Ediacaran body and trace fossils in the Mackenzie Mountains of northwestern Canada. Geol. Soc. Am. Bull. 128 (3–4), 558–575.
Taylor, S.R., McLennan, S.M., 1985. The Continental Crust: its composition and evolution, an examination of the geochemical record preserved in sedimentary rocks. J. Geol. 94, 632–633.
Taylor, S.R., McLennan, S.M., 1995. The geochemical evolution of the continental crust. Rev. Geophys. 33 (2), 241–265.
Tossell, J.A., 2005. Calculating the partitioning of the isotopes of Mo between oxidic and sulfidic species in aqueous solution. Geochim. Cosmochim. Acta 69, 2981–2993.
Tribovillard, N., Riboulleau, A., Lyons, T., Baudin, F., 2004. Enhanced trapping of molybdenum by sulfurized marine organic matter of marine origin in Mesozoic limestones and shales. Chem. Geol. 213, 385–401.
Tribovillard, N., Algeo, T.J., Lyons, T., Riboulleau, A., 2006. Trace metals as paleoredox and paleoproductivity proxies: an update. Chem. Geol. 232, 12–32.
Tyson, R.V., 2001. Sedimentation rate, dilution, preservation and total organic carbon: some results of a modelling study. Org. Geochem. 32, 333–339.
Wang, J., Li, Z.X., 2003. History of Neoproterozoic rift basins in South China: implications for Rodinia break-up. Precambrian Res. 122, 141–158.
Wang, P., Du, Y., Yu, W., Algeo, T.J., Zhou, Q., Xu, Y., Qi, L., Yuan, L., Pan, W., 2020. The chemical index of alteration (CIA) as a proxy for climate change during glacial-interglacial transitions in Earth history. Earth Sci. Rev. 103032.
Wei, G., Wei, W., Wang, D., Li, D., Shields, G.Q., et al., 2020. Enhanced chemical weathering triggered an expansion of euxinic seawater in the aftermath of the Sturtian glaciation. Earth Planet. Sci. Lett. 539, 1–12.
Wen, H., Carignan, J., Zhang, Y., Fan, H., Cloquet, C., Liu, S., 2011. Molybdenum isotopic records across the Precambrian-Cambrian boundary. Geology 39, 775–778.
Wille, M., Nagler, T.F., Lehmann, B., Schroder, S., Kramers, J.D., 2008. Hydrogen sulphide release to surface waters at the Precambrian/Cambrian boundary. Nature 453, 767–769.
Wittkop, C., Swannerb, E.D., Grengs, A., Lambrecht, N., Fakhraee, M., Myrbo, A., Bray, A.W., Poulton, S.W., Katsev, S., 2020. Evaluating a primary carbonate pathway for manganese enrichments in reducing environments. Earth Planet. Sci. Lett. 538.
Wu, C., Zhang, Z., Xiao, J., Fu, Y., Shao, S., Zheng, C., Yao, J., Xiao, C., 2016. Nanhuan manganese deposits within restricted basins of the southeastern Yangtze Platform, China: constraints from geological and geochemical evidence. Ore Geol. Rev. 75, 76–99.
Xiao, J., He, J., Yang, H.Y., 2017. Comparison between Datangpo-type manganese ores and modern marine ferromanganese oxyhydroxide precipitates based on rare earth elements. Ore Geol. Rev. 89, 290–308.
Xu, L., Lehmann, B., Mao, J., 2013. Seawater contribution to polymetallic Ni-Mo-PGE-Au mineralization in Early Cambrian black shales of South China: evidence from Mo isotope, PGE, trace element, and REE geochemistry. Ore Geol. Rev. 52, 66–84.
Ye, Y.T., Wang, H., Zhai, L.N., Wang, X., Wu, C.D., Zhang, S.C., 2018. Contrasting Mo–U enrichments of the basal Datangpo Formation in South China: Implications for the Cryogenian interglacial ocean redox. Precambrian Res. 315, 66–74.
Yu, W., Algeo, T.J., Du, Y., Maynard, B., Guo, H., Zhou, Q., Peng, T., Wang, P., Yuan, L., 2016. Genesis of Cryogenian Datangpo manganese deposit: Hydrothermal influence and episodic post-glacial ventilation of Nanhua Basin, South China. Palaeogeogr. Palaeoclimatol. Palaeoecol. 459, 321–337.
Yu, W., Algeo, T.J., Du, Y., Zhou, Q., Wang, P., Xu, Y., Yuan, L., Pan, W., 2017. Newly discovered Sturtian cap carbonate in the Nanhua Basin, South China. Precambrian Res. 293, 112–130.
Yu, B.S., Dong, H.L., Widom, E., Chen, J.Q., Lin, C.S., 2009. Geochemistry of basal Cambrian black shales and cherts from the Northern Tarim Basin, Northwest China: Implications for depositional setting and tectonic history. J. Asian Earth Sci. 34, 418–436.
Yu, W., Márta, P., Ildikó, G., Krisztián, F., Máté, S., Ivett, K., József, F., Du, Y., Zhou, Q., 2019. Microbial metallogenesis of Cryogenian manganese ore deposits in South China, 459, pp. 122–135.
Yu, W., Algeo, T.J., Zhou, Q., Du, Y., Wang, P., 2020. Cryogenian cap carbonate models: a review and critical assessment. Palaeogeogr. Palaeoclimatol. Palaeoecol. 2020 (552), 109727.
Zhang, F., Zhu, X., Yan, B., Kendall, B., Peng, X., Li, J., Algeo, T.J., Romaniello, S., 2015. Oxygenation of a Cryogenian ocean (Nanhua Basin, South China) revealed by pyrite Fe isotope compositions. Earth Planet. Sci. Lett. 429, 11–19.
Zhou, C., Jiang, S.Y., 2009. Palaeoceanographic redox environments for the lower Cambrian Hetang Formation in South China: evidence from pyrite framboids, redox sensitive trace elements, and sponge biota occurrence. Palaeogeogr. Palaeoclimatol. Palaeoecol. 271, 279–286.
Zhou, C.M., Tucker, R., Xiao, S.H., Peng, Z.X., Yuan, X.L., Chen, Z., 2004. New constraints on the ages of Neoproterozoic glaciations in south China. Geology 32, 437–440.